



Contents lists available at ScienceDirect

Journal of Fluids and Structures

journal homepage: www.elsevier.com/locate/jfs



On the vortex-induced oscillations of a freely vibrating cylinder in the vicinity of a stationary plane wall



Zhong Li^a, Weigang Yao^b, Kun Yang^b, Rajeev K. Jaiman^{b,*}, Boo Cheong Khoo^b

^a NUS Graduate School for Integrative Sciences and Engineering, National University of Singapore, 28 Medical Drive, Singapore 117456, Singapore

^b Department of Mechanical Engineering, National University of Singapore, 21 Lower Kent Ridge Road, Singapore 119077, Singapore

ARTICLE INFO

Article history:

Received 23 January 2016

Received in revised form

13 June 2016

Accepted 1 July 2016

Keywords:

Wall proximity effects
Vortex-induced vibrations
Streamwise oscillation
Beating phenomenon
3D simulations
Streamwise wavelength

ABSTRACT

A partitioned iterative scheme based on Petrov–Galerkin formulation by Jaiman et al. (2016) has been employed for simulating flow past a freely vibrating circular cylinder placed in proximity to a stationary plane wall. In the first part of this work, wall proximity effects on the vortex-induced vibrations (VIV) of an elastically mounted circular cylinder with two degree-of-freedom (2-DoF) are systematically studied in two-dimension (2D) laminar flow at Reynolds number, $Re = 200$ based on the diameter of cylinder. We investigate the hydrodynamic forces, vibration characteristics, phase relations, response frequencies, motion trajectories as well as vortex shedding patterns. For that purpose, a careful comparison has been established between the isolated and near-wall cylinders. Our 2D simulations reveal that (i) the vibrating near-wall cylinder exhibits larger streamwise oscillation and smaller streamwise vibration frequency as compared to its isolated counterpart owing to the energy transfer from fluid to cylinder and streamwise frequency lock-in caused by the suppression of shear layer roll-up from the bottom cylinder surface; (ii) the mechanism of this vortex shedding suppression for the near-wall configuration can be described by a cyclic process where counter-clockwise vortices shed from the bottom surface of the cylinder force the wall boundary layer to separate and induce secondary clockwise vortices which merge with clockwise vortices shed from the upper surface of the cylinder, eventually suppressing the counter-clockwise vortices from the bottom cylinder surface; (iii) beating oscillations during VIV are found at the critical reduced velocities entering and leaving the lock-in region; and (iv) VIV response becomes much more sensitive to the wall proximity in the energy-in phase than in the energy-out phase. In the second part, we perform three-dimensional (3D) simulations for VIV of a circular cylinder for both isolated and near-wall cases at subcritical $Re = 1000$. We compare the hydrodynamic forces and vibration characteristics in 3D with the results corresponding to the 2D study at $Re = 200$. We show that the wall proximity effects on VIV are also pronounced in 3D with the following observations: (i) the wall proximity increases the mean lift force to a lesser extent as compared to 2D at $Re = 200$; (ii) the wall proximity also enhances the streamwise oscillation to a lesser extent as compared to 2D at $Re = 200$; and (iii) the wall proximity increases the wavelength of streamwise vorticity blob.

© 2016 Elsevier Ltd. All rights reserved.

* Corresponding author.

E-mail address: mperkj@nus.edu.sg (R.K. Jaiman).

1. Introduction

The number of untapped onshore hydrocarbon reservoirs has continued to dwindle, leading to a growing need to develop offshore oil and gas technologies. Most of the shallow water hydrocarbons are transported via pipelines to onshore processing facilities. Despite the design and installation difficulties, the pipeline is still a cost effective choice in deep water. The uneven nature of seafloor or possible seabed scouring may cause free spanning along the pipeline. The span length can be easily 100 times that of the pipeline diameter, with a gap from the seabed which can range from essentially zero to more than 2–3 times the pipeline diameter, according to [Sumer and Fredsøe \(2006\)](#). When exposed to flows, free pipeline spans are subjected to dynamic motions induced by currents or waves, referred to as vortex-induced vibrations (VIV), which can cause fatigue related failure of the pipelines. Damage associated with the fatigue of a pipeline undergoing vibrations is known to be proportional to the product of $A^4 f$ where A is the vibration amplitude and f is the vibration frequency, as indicated in [Tsahalis \(1983\)](#). In the short term, small amplitude vibrations with high frequencies may not be detrimental. In the long run, however, they can naturally result in serious consequences due to fatigue. Therefore, the understanding of VIV of a free-span pipeline is of significant importance for offshore industry. The problem of a free-span along the pipeline can be modelled by the configuration in which flow is past an elastically mounted circular cylinder with two degree-of-freedom (2-DoF) in proximity to a stationary plane wall. The numerical studies of VIV of a circular cylinder near a fixed plane wall serve as a foundation to improve pipeline design and installation guidelines.

Most of the previous studies on VIV were generally focused on an isolated circular cylinder placed in a uniform cross-flow without wall proximity effects. There are a number of comprehensive review works on this topic in recent years, such as [Williamson and Govardhan \(2004, 2008\)](#), [Sarpkaya \(2004\)](#), and [Bearman \(2011\)](#). In [Williamson and Govardhan \(2004\)](#), a map of vortex shedding modes (2S, 2P and P+S) was presented. [Sarpkaya \(2004\)](#) summarised the intrinsic nature of VIV of circular cylindrical structures subjected to steady uniform flow. In [Williamson and Govardhan \(2008\)](#), the authors summarised some fundamental results on VIV with low mass and damping with new numerical and experimental techniques. The effects of Reynolds number, Re , on VIV responses of both isolated and tandem cylinders were reviewed in [Bearman \(2011\)](#), in which the Reynolds number based on cylinder diameter D is defined as $Re = U_\infty D/\nu$, where U_∞ denotes the freestream velocity and ν is the kinematic viscosity of the fluid.

Investigations at low Reynolds numbers include the experimental study conducted by [Anagnostopoulos and Bearman \(1992\)](#) in laminar flow at Re from 90 to 150. Direct numerical simulations carried out in low Re regime include [Shiels et al. \(2001\)](#), [Guilmineau and Queutay \(2002\)](#), [Leontini et al. \(2006\)](#), and [Prasanth and Mittal \(2009\)](#). In the work by [Shiels et al. \(2001\)](#), the dimensionless peak transverse oscillation amplitude is 0.59 for a massless cylinder with 1-DoF motion, achieving a good agreement with experimental results ([Anagnostopoulos and Bearman, 1992](#)). The vortex sheddings of a forced streamwisely oscillating cylinder in water at rest with $Re=100$ and $KC = U_\infty T/D = 5$ (where T denotes the period of oscillation) and a forced transversely oscillating cylinder in a uniform flow at $Re=185$ were numerically investigated in [Guilmineau and Queutay \(2002\)](#). In [Leontini et al. \(2006\)](#), the authors performed 2D simulations at $Re=200$ and found that the genesis of the higher- Re flow behaviour is also present in low- Re 2D flow in terms of regimes of cylinder response, frequency and phase response of the cylinder. The authors ([Prasanth and Mittal, 2009](#)) numerically studied VIV of two circular cylinders in both tandem and staggered arrangements using a stabilized finite element method in 2D at $Re=100$.

The authors ([Khalak and Williamson, 1999](#)) found that the cylinder response can be characterised by two types of VIV behaviour. With a low mass damping, there are three distinct branches in the response curve with the variation of reduced velocity. The three branches are termed as the initial, upper and lower branches. With high mass damping, the upper branch does not exist. The distinct branches in the response curve are associated with different vortex shedding modes at the wake region of the cylinder. [Govardhan and Williamson \(2000\)](#) found that for 1-DoF vibrating cylinder with high mass damping, two branches of the response are found, namely the initial and lower branches. The vortex wake on the initial branch comprises a 2S mode while a 2P mode is shown on the lower branch. [Jeon and Gharib \(2001\)](#) found that in 2-DoF VIV the streamwise displacement inhibits the formation of the 2P vortex shedding mode.

The proximity of a plane wall introduces complications to the vortex shedding in the wake. One of the earliest experiments studying ground effect on a circular cylinder was reported by Taneda's experiment ([Taneda, 1998](#)), where the flow behind a circular cylinder towed through stagnant water close to a fixed ground was visualised at $Re=170$. The water and ground moved together relative to the cylinder and thus there was essentially no boundary layer formed on the ground. Regular alternate vortex shedding occurred at a gap ratio, e/D where e denotes the gap distance, of 0.6, while only a weak single row of vortices was shed at $e/D = 0.1$.

When the wall in proximity is stationary, a boundary layer forms along the wall. The development of three shear layers is involved, namely the two separated from the upper and lower sides of the cylinder, as well as the wall boundary layer. [Bearman and Zdravkovich \(1978\)](#) showed that the vortex shedding is suppressed if e/D is small enough. Studies by [Zdravkovich \(1985\)](#) and [Lin et al. \(2005\)](#), carried out at $Re=3550$ and 780, respectively, showed the cessation of regular vortex shedding for a stationary cylinder near a fixed plane wall. Other studies of stationary cylinder near a fixed wall by [Lei et al. \(2000\)](#) and [Wang and Tan \(2008\)](#) showed that Re , e/D and boundary layer thickness, δ/D , are parameters affecting the flow for a cylinder near a fixed wall. [Ong et al. \(2008\)](#) applied the standard high Reynolds number $k-\omega$ model at $Re = 1.0 \times 10^4$ – 4.8×10^4 with $\delta/D = 0.14$ –2, finding that under-predictions of the essential hydrodynamic quantities were observed in the subcritical flow regime due to the limited capacity of the $k-\epsilon$ model in capturing the vortex shedding correctly. [Ong et al. \(2010\)](#) carried out numerical studies on stationary near-wall cylinder in the turbulent regime. For the

stationary near-wall cylinder, it was found that the C_D increases as e/D increases for small e/D , reaching a maximum value before decreasing to a constant.

When the wall in proximity is moving at the freestream velocity, no wall boundary layer is formed. Huang and Hyung (2007) used immersed boundary method (IBM) to study the critical gap ratio for $Re=300, 400, 500$ and 600 , observing an inverse relation between the critical e/D and Reynolds number. They further concluded that the critical gap ratio corresponds to a local minimum of the streamwise maximum mean velocity in the gap. In Rao et al. (2013), the researchers conducted numerical investigations on the dynamics and stability of the flow past two tandem cylinders sliding along a wall for $20 \leq Re \leq 200$. Li et al. (2016) numerically investigated shear-free wall proximity effects at low Reynolds numbers for flow past a circular cylinder placed in the vicinity of a plane moving wall. The dynamics of the tandem cylinder arrangement near to a moving wall was reported at low Re in D'souza et al. (2016).

Due to the effect of wall proximity, the dynamics of VIV is much more complex than freely vibrating cylinder in a freestream flow. For vibrating near-wall cylinder, the vortex shedding may occur even at very small gap ratio as compared to the stationary counterparts, according to Fredsøe et al. (1987) and Raghavan et al. (2009). Investigations for vibrating cylinder near a plane wall were mainly conducted in the moderate to high Re regime, including those by Kozakiewicz et al. (1992) and Tsalalis and Jones (1981), which showed that the XY-trajectory of a near-wall cylinder is an oval-shape, instead of the common figure-of-eight shape observed in vibrating isolated cylinder. Fredsøe et al. (1985) found that the transverse vibration frequency is close to the vortex shedding frequency of a stationary cylinder when reduced velocity, $U_r = U_\infty/f_n D$ where f_n is the natural frequency, $U_r < 3$ and $e/D > 0.3$. When $3 < U_r < 8$, the transverse vibrating frequency deviates considerably from the vortex shedding frequency of a stationary cylinder. Taniguchi and Miyakoshi (1990) reported the fluctuations of lift and drag on the cylinder under the wall proximity effects by looking into e/D and δ/D at $Re = 9.4 \times 10^4$. It is assumed that Kármán vortex streets are formed by concentrations of vorticity due to the rolling-up of separated shear layers which issued from both sides of the cylinder. They pointed out that the concentration of vorticity was reduced and formation of the Kármán vortex streets was interrupted by the gap flow at small gap ratios based upon their flow visualisations.

Brørs (1999) and Zhao et al. (2007) utilised $k-\epsilon$ model at $Re = 1.5 \times 10^4$ and a $k-\omega$ model at $Re = 2.0 \times 10^4$, respectively. Their results agreed well with the experimental data available. Zhao and Cheng (2011) studied numerically 2-DoF VIV of near-wall cylinder in the turbulent regime. Their study investigates low gap ratios of $e/D = 0.002$ and 0.3 , where effects of bounce-back from the plane boundary on the VIV are studied. Wang and Tan (2013) conducted an experimental study for a 1-DoF vibrating cylinder near a plane wall at $3000 \leq Re \leq 13,000$ and a low mass ratio $m^* = (4m)/(\pi\rho D^2)$, where m denotes the mass of cylinder and ρ denotes the density of fluid, of 1.0 for $1.53 \leq U_r \leq 6.62$. It was demonstrated that the nearby wall not only affects the amplitude and frequency of vibration, but also leads to non-linearities in the cylinder response as evidenced by the presence of super-harmonics in the drag force spectrum. The vortices shed that would otherwise be in a double-sided vortex street pattern are arranged into a single-sided pattern, as a result of the wall. Tham et al. (2015) presented a numerical study on VIV of a freely vibrating 2-DoF circular cylinder in close proximity to a stationary plane wall at $Re=100$. They reported that the effect of wall proximity tends to disappear for $e/D \geq 5$ and proposed new correlations for characterizing peak amplitudes and forces as a function of the gap ratio.

The literature review above indicates that previous research on near-wall stationary and vibrating cylinder focused primarily on moderate to high Re regime. However, few works on numerical studies of 2-DoF VIV of an elastically supported circular cylinder in proximity to a wall in the low Re regime can be found in the literature. As it is known that the branching of cylinder response for VIV has its genesis in two-dimensional low Re flow and the essential aspects of VIV dynamics can be captured numerically at lower Re , as reported in Leontini et al. (2006) as well as Mysa et al. (2016). The primary aim of this study is to investigate the effects of the wall proximity on VIV of an elastically mounted circular cylinder with 2-DoF by characterizing the hydrodynamic forces, the vibration responses, the phase differences between the hydrodynamic forces and displacements as well as the vortex shedding patterns for both the near-wall and isolated cases in both 2D and 3D. In the neighbourhood of a stationary wall, the vortex dynamics and response characteristics are quite different from that of the isolated cylinder vibrating in a freestream flow. In particular, we investigate the origin of enhanced streamwise vibrations of near-wall cylinder as compared to the freely vibrating isolated cylinder configuration. This study represents a step towards an improved understanding of vibrations of subsea pipelines subject to ocean currents with varying gaps from the seabed. An understanding of the mechanism of the large seabed-induced streamwise vibrations may improve future design of the subsea pipelines and may pave the way to design more effective suppression devices.

The remainder of this paper is organised as follows. The governing equations and the numerical method employed in this work are presented in Section 2. The problem definition and the convergence study are described in Section 3. This is followed by the results for 2D simulations in Section 4. In this section, we present the characterisation of the response dynamics of isolated and near-wall cylinders and discuss the basic differences between the two arrangements in terms of wake topology, response dynamics, force components, phase and frequency characteristics. The results for 3D near-wall VIV simulations are presented in Section 5 for representative reduced velocities and contrasted against the isolated counterpart. Lastly, the major conclusions of this study are provided in Section 6.

2. Numerical formulation

The Navier–Stokes equations governing an incompressible Newtonian flow in an arbitrary Lagrangian–Eulerian reference frame are

$$\rho^f \frac{\partial \mathbf{u}^f}{\partial t} + \rho^f (\mathbf{u}^f - \mathbf{w}) \cdot \nabla \mathbf{u}^f = \nabla \cdot \boldsymbol{\sigma}^f + \mathbf{b}^f \quad \text{on } \Omega^f(t), \quad (1)$$

$$\nabla \cdot \mathbf{u}^f = 0 \quad \text{on } \Omega^f(t), \quad (2)$$

where \mathbf{u}^f and \mathbf{w} represent the fluid and mesh velocities, respectively, \mathbf{b}^f is the body force applied on the fluid and $\boldsymbol{\sigma}^f$ is the Cauchy stress tensor for a Newtonian fluid written as

$$\boldsymbol{\sigma}^f = -p\mathbf{I} + \mu^f \left(\nabla \mathbf{u}^f + (\nabla \mathbf{u}^f)^T \right). \quad (3)$$

Here, p is pressure in the fluid, \mathbf{I} is the identity tensor and μ^f is the fluid viscosity. The fluid stress tensor $\boldsymbol{\sigma}^f$ is considered as a sum of a pressure contributed stress component $\boldsymbol{\sigma}_p$ and a viscous contributed stress component $\boldsymbol{\sigma}_\mu$ which are given as

$$\boldsymbol{\sigma}_p = -p\mathbf{I}, \quad (4)$$

$$\boldsymbol{\sigma}_\mu = \mu^f \left(\nabla \mathbf{u}^f + (\nabla \mathbf{u}^f)^T \right). \quad (5)$$

A cylinder body submerged in the flow stream experiences transient vortex-induced forces and consequently may undergo rigid body motion if mounted elastically. The rigid-body motion of the cylinder in the two directions along the Cartesian axes, is governed by the following equation:

$$\mathbf{m} \frac{\partial \mathbf{u}^s}{\partial t} + \mathbf{c} \cdot \mathbf{u}^s + \mathbf{k} \left(\phi^s(\mathbf{z}_0, t) - \mathbf{z}_0 \right) = \mathbf{F}^s + \mathbf{b}^s \quad \text{on } \Omega^s, \quad (6)$$

where \mathbf{m} , \mathbf{c} and \mathbf{k} denote the mass, damping and stiffness vectors per unit length for the translational degrees of freedom, Ω^s denotes the rigid body, $\mathbf{u}^s(t)$ represents the rigid-body velocity at time t , \mathbf{F}^s and \mathbf{b}^s are the fluid traction and body forces acting on the rigid body, respectively. Here ϕ^s denotes the position vector mapping the initial position \mathbf{z}_0 of the rigid body to its position at time t . The spatial and temporal coordinates are denoted by \mathbf{x} and t , respectively. The coupled system requires to satisfy the no-slip and traction continuity conditions at the fluid–body interface Γ as follows:

$$\mathbf{u}^f(\phi^s(\mathbf{z}_0, t), t) = \mathbf{u}^s(\mathbf{z}_0, t), \quad (7)$$

$$\int_{\phi^s(\gamma, t)} \boldsymbol{\sigma}^f(\mathbf{x}, t) \cdot \mathbf{n} d\Gamma + \int_\gamma \mathbf{F}^s d\Gamma = 0 \quad \forall \gamma \in \Gamma, \quad (8)$$

where \mathbf{n} is the outer normal to the fluid–body interface, γ is any part of the fluid–body interface Γ_f in the reference configuration, $d\Gamma$ denotes a differential surface area and $\phi^s(\gamma, t)$ is the corresponding fluid part at time t . In Eq. (8), the first term represents the force exerted by the fluid on $\phi^s(\gamma, t)$, while the second term represents the net force by the rigid body.

A solver using Petrov–Galerkin finite-element and semi-discrete time stepping has been employed to investigate the interaction of incompressible viscous flow with rigid-body dynamics of freely vibrating cylinder. To account for fluid–rigid body interaction, a partitioned iterative scheme based on nonlinear interface force correction (Jaiman et al., 2016) has been employed for stable and accurate coupling with strong added mass effects. The temporal discretization of both the fluid and the structural equations is embedded in the generalised- α framework by making use of classical Newmark approximations in time (Chung and Hulbert, 1993). Throughout this study, the incremental velocity and pressure are computed via the matrix-free implementation of the restarted Generalised Minimal Residual (GMRES) solver proposed in Saad and Schultz (1986). The GMRES uses a diagonal preconditioner and a Krylov space of 30 orthonormal vectors. In the current formulation, we perform Newton–Raphson type iterations to minimise the linearization errors per time step.

The fluid loading is computed by integrating the surface traction considering the first layer of elements located on the cylinder surface. The instantaneous force coefficients are defined as

$$C_L = \frac{1}{\frac{1}{2}\rho^f U_\infty^2 D} \int_\Gamma (\boldsymbol{\sigma}^f \cdot \mathbf{n}) \cdot \mathbf{n}_y d\Gamma, \quad C_D = \frac{1}{\frac{1}{2}\rho^f U_\infty^2 D} \int_\Gamma (\boldsymbol{\sigma}^f \cdot \mathbf{n}) \cdot \mathbf{n}_x d\Gamma, \quad (9)$$

where ρ^f and $\boldsymbol{\sigma}^f$ denote fluid density and stress, respectively, and \mathbf{n}_x and \mathbf{n}_y are the Cartesian components of the unit normal, \mathbf{n} . In the present study, C_D and lift coefficient C_L are post-processed using the conservative flux extraction of nodal tractions along the fluid–body interface.

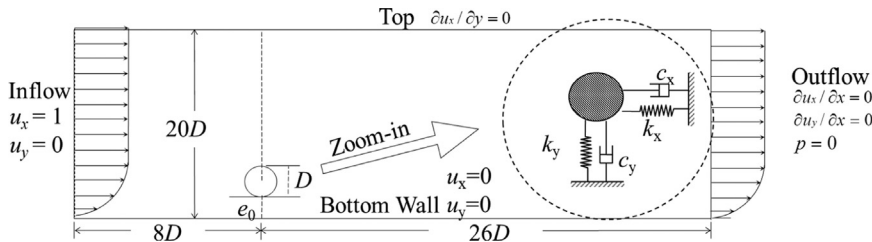


Fig. 1. Schematic of 2D computational domain with details of boundary conditions.

3. Problem definition and convergence study

3.1. Model description

The 2D computational domain is depicted in Fig. 1 to illustrate the domain and boundary conditions details. A circular cylinder is placed in the vicinity of a plane wall and the centre of the cylinder is at a distance of $8D$ to the inflow boundary and of $26D$ to the outflow boundary, allowing sufficient distances in capturing the vortex dynamics in the downstream wake. The adequacy of similar boundary locations was demonstrated in earlier works in Prasanth and Mittal (2008), Navrose and Mittal (2013) and Jaiman et al. (2016).

The width of the computational domain is $20D$, thereby the resulting blockage based on the diameter of the cylinder and the lateral dimension of the domain is 5%. The same blockage was also used in Navrose and Mittal (2013). For the isolated configuration, the lateral boundaries are each $10D$ away from the cylinder centre, with slip boundary conditions applied on both top and bottom walls, i.e. $\partial u_x/\partial y = 0$. For the near-wall configuration, in which the bottom boundary serves as a stationary rigid wall, the distance between the lower surface of the cylinder and the bottom wall is governed by the gap ratio, denoted by e/D , with e being the initial gap distance. The centre of the near-wall cylinder is then located at $(0.5D + e)$ to the bottom boundary, as shown in Fig. 1. The boundary conditions are described as follows for the near-wall configuration: at the inlet, a Dirichlet velocity for the steady incoming flow is given with $u_x=1$ and $u_y=0$ to represent the free stream; at the outlet, a traction free condition is imposed as $\partial u_x/\partial x = 0$ and $\partial u_y/\partial x = 0$ for velocities and $p=0$ for the pressure equation; at the top a free-slip boundary condition is applied by $\partial u_x/\partial y = 0$ and $u_y=0$; for the cylinder surface and the bottom wall, a no-slip boundary condition is imposed by setting $u_x=0$ and $u_y=0$. The mesh movement method involved has been designed in such a way that the mesh surrounding the cylinder moves along with it like a rigid body while there is an outer boundary remaining stationary, shown in Fig. 2.

A few simulations are performed using three-dimensional stabilized finite element formulation to investigate the 3D effects on freely vibrating cylinders. The 3D domain, as shown in Fig. 3, is simply an extrusion of the 2D plane along the cylinder axis (z -axis). In addition to the boundary conditions applied at the 2D domain, for the 3D domain, a periodic boundary condition is applied at the two ends of the cylinder (front and back sides of the 3D domain) to model a cylinder of infinite length. The 3D calculations are conducted for a cylinder with a spanwise length (in z direction) of $5D$, which is larger than the spanwise length of $4D$ used by Navrose and Mittal (2013) for the same Reynolds number.

3.2. Cylinder VIV modelling

A rigid circular cylinder is mounted elastically by springs and dampers and allowed to vibrate freely in both transverse (y -axis) and streamwise (x -axis) directions. The structural property of the cylinder is depicted in the dashed circles in both Figs. 1 and 3. Both the transverse and streamwise springs are assumed to be linear and homogeneous in the stiffness, yielding

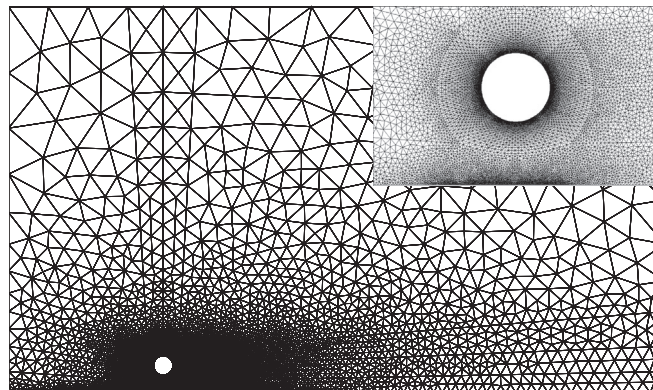


Fig. 2. Two-dimensional mesh used in simulations for the near-wall configuration with the zoom-in view on the cylinder.

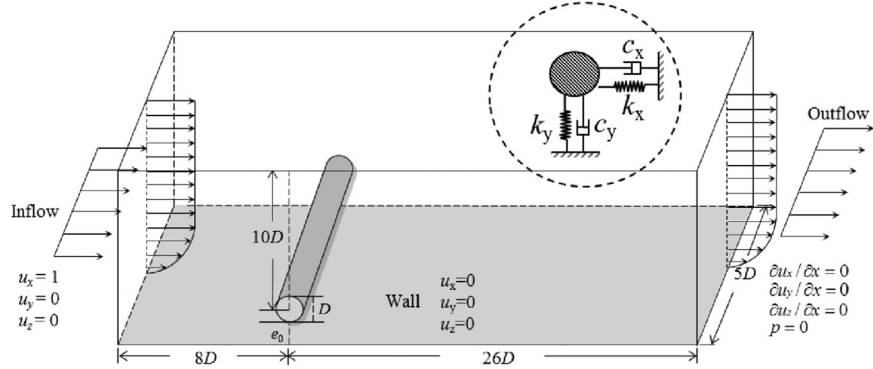


Fig. 3. Schematic of the 3D computational domain with details of boundary conditions.

identical natural frequencies in both directions, so the ratio of f_{nx} to f_{ny} is unity. Computations are carried out for various reduced velocities for a fixed mass ratio of the cylinder, $m^* = (4m)/(\pi\rho D^2) = 10$ where m is the cylinder mass and ρ is the fluid density, at given Re . The reduced velocity is defined as $U_r = \frac{U_\infty}{f_n D} = \frac{U_\infty}{\frac{1}{2\pi}\sqrt{\frac{k}{m}} D}$. Therefore, U_r is adjusted by varying the spring stiffness, k , and thus

varying f_n of the cylinder. One characteristic feature of VIV is frequency lock-in, and the key parameter for the frequency lock-in phenomenon in VIV is the natural frequency of the system f_n . In [de Langre \(2006\)](#), the author postulated that the mechanism underlying the lock-in of frequencies in VIV is coupled wake dynamics mode and solid dynamics mode flutter using an elementary linear model. In a recent work ([Zhang et al., 2015](#)), the authors pointed out that the mechanism of frequency lock-in at low Re can be divided into two modes: flutter-induced (coupled wake mode and structure mode instability) and resonance-induced (only wake mode instability) using numerical simulations. The definitions of the VIV quantities used in the present analysis are described as follows. The coefficients of mean lift \bar{C}_L and mean drag \bar{C}_D are evaluated as

$$\bar{C}_L = \frac{1}{n} \sum_{i=1}^{i=n} C_{L,i}, \quad \bar{C}_D = \frac{1}{n} \sum_{i=1}^{i=n} C_{D,i} \quad (10)$$

whereby their root-mean-square (rms) counterparts are

$$(C_L)_{rms} = \sqrt{\frac{1}{n} \sum_{i=1}^{i=n} (C_{L,i} - \bar{C}_L)^2}, \quad (C_D)_{rms} = \sqrt{\frac{1}{n} \sum_{i=1}^{i=n} (C_{D,i} - \bar{C}_D)^2} \quad (11)$$

and the maximum and rms amplitudes are defined as

$$(A_y)_{max}/D = \frac{1}{2} |(A_y)_{max} - (A_y)_{min}|/D, \quad (A_x)_{rms}/D = \left[\sqrt{\frac{1}{n} \sum_{i=1}^{i=n} (A_{x,i} - \bar{A}_x)^2} \right] / D \quad (12)$$

where n denotes the number of samples taken.

3.3. Grid convergence study

A mesh independent study is carried out in this section. The domain is discretized using an unstructured finite-element mesh, which provides a flexibility to design finer grid resolutions in the high gradient regions and a coarse grid in the far-field regions. All the meshes evaluated are given in [Tables 1](#) and [2](#). The mesh convergence study involves two steps: firstly, a 2D mesh is chosen by assessing different 2D meshes; secondly, the 3D mesh is generated by layering the 2D mesh along the spanwise direction (z-axis). The effects of the spanwise resolution, $\Delta z/D$, are then taken into account to determine a suitable mesh to be used for 3D simulations.

The first step evaluates three 2D meshes of different resolutions. In order to quantify the dependency of the numerical results on the mesh density, numerical simulations are conducted at three meshes with different densities as shown in [Table 1](#). The calculations are performed for an isolated circular cylinder of $m^* = 10$ with 2-DoF at $Re = 200$ and $U_r = 5$. At this particular reduced velocity, high vibration amplitudes are expected along with the sensitive nature of amplitude response on numerical discretization errors. For different meshes, we have calculated the representative hydrodynamic forces and cylinder responses undergoing free vibrations subjected to the incoming flow.

Results from different meshes are summarised in [Table 1](#). With Mesh C being the reference, the differences between results from Mesh A and Mesh B and those from Mesh C are thus calculated and noted in the corresponding brackets. It is shown in [Table 1](#) that differences between the results are approximately within 1% for the two finer meshes, Mesh B and Mesh C. Considering the

Table 1Grid convergence study of 2D simulations for an isolated cylinder at $Re=200$ and $U_r = 5$.

Mesh	N_{cyl}^*	N_{e2D}^*	\bar{C}_D	$(C_L)_{rms}$	$(A_x)_{rms}/D$	$(A_y)_{max}/D$
A	128	21,612	2.1311 (3.70%)	0.0924 (3.47%)	0.0092 (5.75%)	0.5693 (3.55%)
B	168	25,988	2.0645 (0.46%)	0.0901 (0.89%)	0.0088 (1.15%)	0.5548 (0.91%)
C	200	32,477	2.0551	0.0893	0.0087	0.5498

* N_{cyl} : number of points around the cylinder circumference; N_{e2D} : total number of elements in 2D domain.

computational efficiency, Mesh B is then selected as the mesh to perform our 2D simulations. The accuracy of our implementation using Mesh B is assessed by comparing the present results with [Leontini et al. \(2006\)](#) in [Section 4.2](#).

By a similar process, the second step for the grid convergence study is conducted for a 3D modelling of VIV of an isolated cylinder at $Re=1000$ and $U_r=5$. Using the 2D mesh selected, different spanwise resolutions are assessed, namely $\Delta z'/D = 0.5, 0.2$ and 0.1 . The results obtained for different $\Delta z'/D$ are given in [Table 2](#). Comparing the results in [Table 2](#), it is seen that the spanwise resolution has an obvious influence on the results. Also, the guidelines of spanwise resolution used in 3D studies can be found in relevant references. [Navrose and Mittal \(2013\)](#) used a spanwise resolution of 0.08 for the same Re and m^* . In [Zhao et al. \(2014\)](#), a spanwise resolution of 0.1 is utilised for VIV of a vertical circular cylinder with a mass ratio of $m^* = 2$ at $Re=1000$. Thus, following the guidelines, for the 3D calculations in the present study, Mesh B3 with the finest spanwise resolution of $\Delta z'/D = 0.1$ is then considered for this study. It is also noted that the time step size used in both 2D and 3D simulations is $\Delta t = 0.05$. A systematic temporal convergence study has been performed for VIV in [Jaiman et al. \(2016\)](#), which utilises the same numerical scheme.

4. Two-dimensional results and discussion

Two-dimensional simulations of VIV of an elastically mounted circular cylinder of $m^* = 10$ with 2-DoF have first been performed at $Re=200$ for U_r ranging from 3 to 9 with an interval of 0.5. Definitions of the governing parameters and corresponding values for the 2D studies are listed in [Table 3](#). For the near-wall cylinder, the initial gap ratio is $e/D = 0.90$, which is large enough to prevent the cylinder from contacting the bottom wall during VIV. For the purpose of studying the wall proximity effects, VIV of an isolated cylinder, i.e. $e/D = \infty$, is compared with the results of the near-wall configuration. All 2D cases have been simulated until dimensionless time $tU/D = 500$. The results presented in the following are extracted from the dimensionless time range $tU/D = 250 – 500$.

4.1. Hydrodynamic forces

For a self-excited cylinder undergoing free vibrations, the vortex shedding due to complex interaction between the shear layers and the near wake leads to oscillating hydrodynamic forces which serve as the exciting forces. It is important to understand the unsteady fluid loads over vibrating bodies. The mean and root-mean-squared lift coefficient, \bar{C}_L and $(C_L)_{rms}$, as well as the mean and root-mean-squared drag coefficient, \bar{C}_D and $(C_D)_{rms}$, for both the near-wall cylinder and the reference isolated cylinder with the variation of U_r are presented in [Fig. 4a](#) and b, respectively. It is apparent that the wall proximity greatly increases the \bar{C}_L for all U_r values considered herein. This is because the increase in the transverse force coefficient is associated with the breaking of the symmetric flow fields by the wall presence which yields a non-zero \bar{C}_L on the cylinder. This phenomenon has already been reported in [Tham et al. \(2015\)](#) for the low Re regime and in [Ong et al. \(2010\)](#) for the subcritical regime. As seen in [Fig. 4a](#), the largest increase in \bar{C}_L due to wall proximity takes place over the lock-in region where the cylinder undergoes vibrations of large amplitude. The increase of \bar{C}_L in the lock-in region is also a result from the increased transverse vibration in the lock-in region, seen in [Fig. 5a](#) where $(A_y)_{max}/D$ peaks at $U_r = 4.5$, and so does \bar{C}_L in [Fig. 4a](#). As the transverse vibration amplitude peaks, the cylinder vibrates closest to the wall, leading to the most

Table 2Grid convergence study of 3D simulations for an isolated cylinder at $Re=1000$ and $U_r = 5$.

Mesh	$\Delta z'/D$	N_{e3D}^*	\bar{C}_D	$(C_L)_{rms}$	$(A_x)_{rms}/D$	$(A_y)_{max}/D$
B1	0.5	313,168	1.6671 (5.70%)	0.1066 (6.28%)	0.0089 (8.54%)	0.6050 (5.54%)
B2	0.2	709,276	1.6105 (2.11%)	0.1027 (2.39%)	0.0084 (2.44%)	0.5849 (1.32%)
B3	0.1	1,366,576	1.5772	0.1003	0.0082	0.5773

* N_{e3D} : total number of elements in 3D domain.

Table 3

Key VIV parameters for 2D simulations.

Parameter	Symbols	Definitions	Value
Mass ratio	m^*	$4m/(\pi\rho D^2)$	10
Reduced velocity	U_r	$U_\infty/(f_n D)$	3–9
Damping ratio	ζ	$c/2\sqrt{km}$	0, 0.01
Reynolds number	Re	$U_\infty D/\nu$	200
Initial gap ratio	e/D	e/D	0.9, ∞

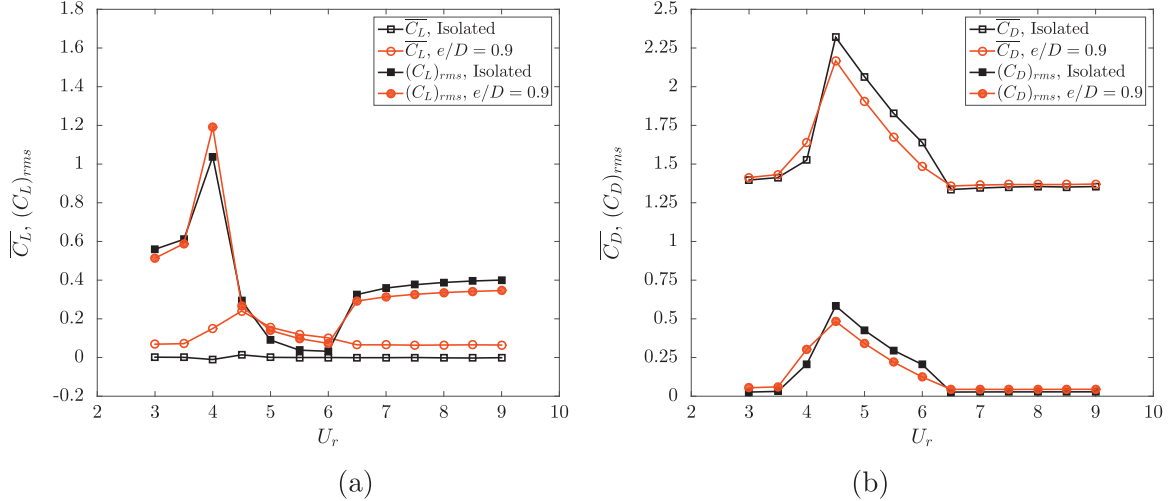


Fig. 4. Force coefficients as a function of reduced velocity U_r for both isolated and near-wall cylinders at $Re=200$: (a) mean lift coefficient \bar{C}_L , root-mean-squared lift coefficient $(C_L)_{rms}$, (b) mean drag coefficient \bar{C}_D , root-mean-squared drag coefficient $(C_D)_{rms}$.

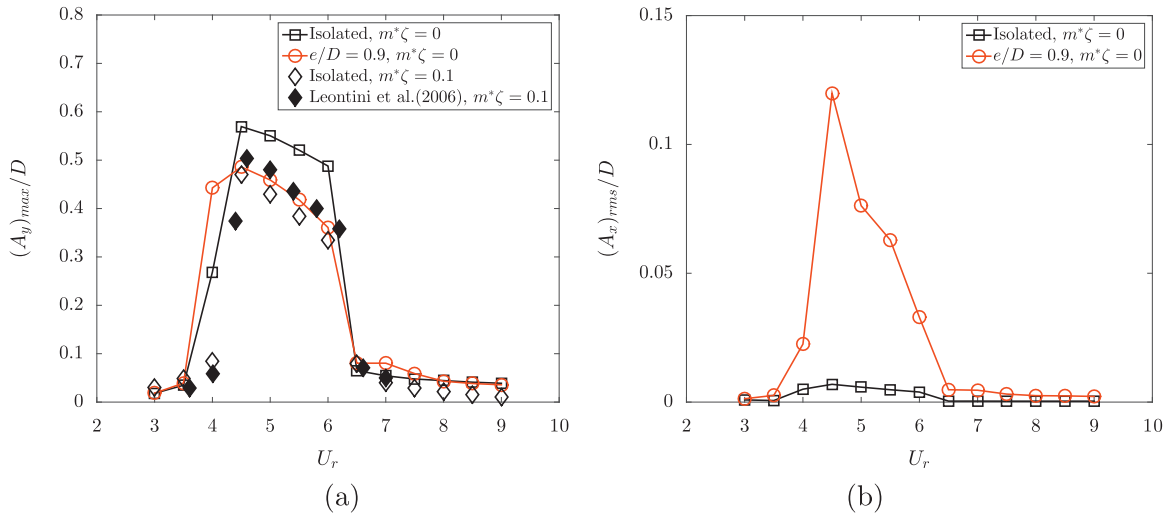


Fig. 5. Vibration amplitudes as a function of reduced velocity U_r for both isolated and near-wall cylinders at $Re=200$: (a) normalised maximum transverse displacement $(A_y)_{max}/D$, (b) normalised root-mean-squared streamwise displacement $(A_x)_{rms}/D$.

unsymmetrical flow field at the smallest instantaneous gap thereby \bar{C}_L becomes the largest. It can also be observed that the wall proximity does not affect $(C_L)_{rms}$ much as the trend of the near-wall cylinder follows closely with that of the isolated configuration. It is also noted that $(C_L)_{rms}$ has a small jump from the lock-in regime to the post-lock-in. This jump in $(C_L)_{rms}$ is also reported in Tham et al. (2015) for the isolated cylinder.

In the lock-in range, it is found that wall proximity causes a substantial increase in \bar{C}_L while a slight decrease in both \bar{C}_D and $(C_D)_{rms}$ in general. For both configurations, the drag forces are relatively much larger in the lock-in as compared to the lock-in free regime. As reported earlier in Zdravkovich (1985) and Jensen et al. (1990), in general, a neighbouring wall has a

Table 4Comparison of $[(A_y)_{max}/D]^*$ with reference studies at low Re .

Category	Study	Re	$m^*\zeta$	$[(A_y)_{max}/D]^*$
Numerical	Blackburn and Kar-niadakis (1993)	200	0.012	0.64
	Newman and Kar-niadakis (1995)	200	0	0.65
	Fujarra et al. (1998)	200	0.015	0.61
	Leontini et al. (2006)	200	0.1	0.51
	Guilmineau and Queuey (2000)	100	0.0179	0.54
	Shiels et al. (2001)	100	0	0.59
	Tham et al. (2015)	100	0	0.57
Experimental	Anagnostopoulos and Bearman (1992)	90–150	0.179	0.64
	Present	200	0	0.57
	Present	200	0.1	0.49

decreasing effect on the mean drag, which is consistent with the present study. Shown in Fig. 4b, the decrease in $\overline{C_D}$ is most obvious in the lock-in range. To be specific, $\overline{C_D}$ for the near-wall case is approximately 90% that of the isolated cylinder. However, with the presence of the plane wall, although $\overline{C_L}$ has a large difference, the change in transverse displacement is small, shown in Fig. 5a. On the contrary, although $\overline{C_D}$ and $(C_D)_{rms}$ have little difference, the streamwise response is greatly enlarged by the wall proximity, as shown in Fig. 5b. This suggests that stark differences in the streamwise oscillations between near-wall and isolated cases are not due to the difference in the streamwise forces. Reasons for the enhanced streamwise oscillations in Fig. 5b are discussed in Sections 4.3 and 4.4.

4.2. Cylinder response amplitudes

Fig. 5 summarizes the normalised maximum transverse displacements, $(A_y)_{max}/D$, and the normalised root-mean-squared streamwise displacements, $(A_x)_{rms}/D$, for both the isolated and near-wall cylinders as a function of U_r . In Fig. 5a, to verify the accuracy of our implementation, $(A_y)_{max}/D$ for the VIV of an isolated cylinder with the mass damping of $m^*\zeta = 0.1$ (i.e. $m^* = 10$ and $\zeta = 0.01$) is first compared with the results from Leontini et al. (2006), and our $(A_y)_{max}/D$ agrees well with the reference data. For the case of $m^*\zeta = 0$, the results of $(A_y)_{max}/D$ for both isolated and near-wall configurations are also shown in Fig. 5a. To further assess the accuracy, the peak normalised maximum transverse displacement over the whole range of U_r , $[(A_y)_{max}/D]^*$, in the present 2D simulations is also benchmarked with some other studies. The comparison of $[(A_y)_{max}/D]^*$ is tabulated in Table 4.

It is shown in Fig. 5a that the lock-in region approximately ranges from $U_r = 4$ to 6.5, where the cylinder undergoes large-amplitude vibrations. The lock-in state of the freely oscillating rigid cylinder is first described by a two-branch response as documented in the experiments of Brika and Laneville (1993) as well as Khalak and Williamson (1996): an upper branch that corresponds to large amplitude and low values of reduced velocity, and a lower branch that corresponds to low amplitudes and large values of reduced velocity. Prasanth and Mittal (2008) found that, unlike high Re VIV, low Re VIV only exhibits two branches, namely “initial” and “lower”. In Fig. 5a, in the lock-in region, the cylinder response is clearly characterised by two branches: initial and lower. The range of $U_r \leq 3.5$ represents the pre-lock-in regime, where the vibration amplitudes are negligibly small. As U_r increases, the vortex shedding frequency synchronizes with the cylinder vibration frequency, and the lock-in range is then entered. In the initial branch of the lock-in, the vibration amplitude increases dramatically as U_r increases before reaching a peak value. The maximum amplitude $(A_y)_{max}/D$ then decreases gently as U_r increases prior to decreasing sharply in the lower branch of the lock-in range. As U_r continues increasing when $U_r \geq 7$, the post-lock-in region is then entered. It is also observed in Fig. 5a that the $(A_y)_{max}/D$ of the near-wall cylinder behaves similarly with its isolated counterpart, thus the wall proximity does not significantly alter the behaviour of the transverse response. On the contrary, in Fig. 5b, $(A_x)_{rms}/D$ of the near-wall cylinder is by far larger than that of the isolated cylinder, particularly in the lock-in region. The maximum amplitude $(A_x)_{rms}/D$ of the near-wall cylinder is as large as approximately 17 times that of the isolated cylinder. It can be easily deduced here that the wall proximity has a much larger effect in the streamwise direction than the transverse direction, and this wall proximity effect is most pronounced in the lock-in regime.

Further, the influence of the wall proximity on the cylinder response shows an inverse trend with that of the hydrodynamic forces. In the earlier discussion, the wall proximity largely enhances the hydrodynamic force on the transverse direction, i.e. $\overline{C_L}$, but has little effect in the streamwise direction, i.e. $\overline{C_D}$, as shown in Fig. 4. In summary, the major influence of wall proximity is a large enhancement in the streamwise response with little effect on the transverse response; as well as a large increase in the transverse force with little effect on the streamwise force. This shows that the large enhancement in the streamwise response by the wall proximity is not because of the increase in the hydrodynamic force in the streamwise

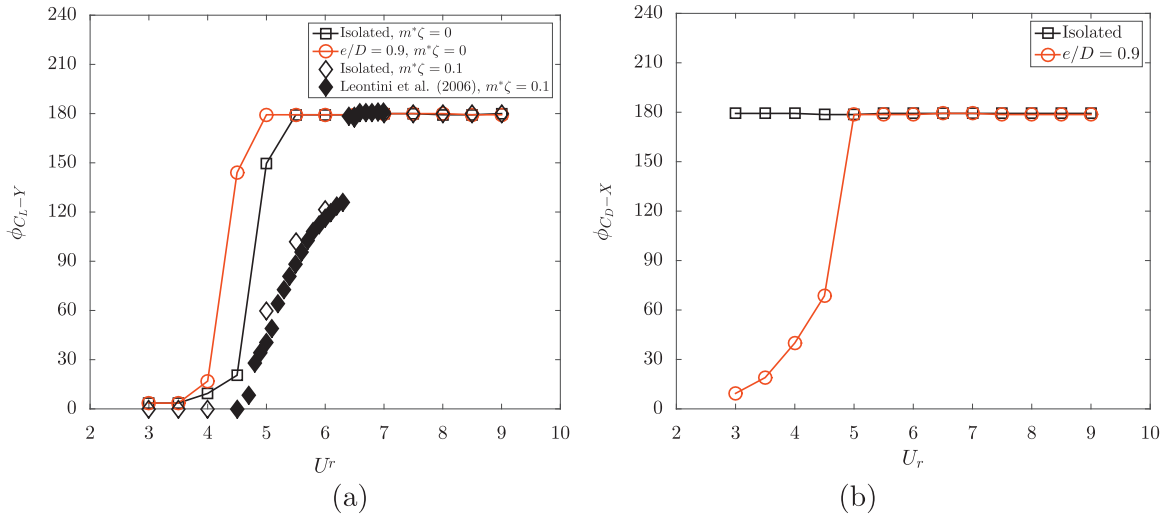


Fig. 6. Phase relations as a function of reduced velocity U_r for isolated and near-wall cylinders at $Re=200$: (a) ϕ_{C_L-Y} between lift and transverse displacement, (b) ϕ_{C_D-X} between drag and streamwise displacement.

direction. Therefore, in the following section, we will investigate why the streamwise response of the near-wall cylinder is largely enhanced compared to its isolated counterpart.

4.3. Phase relations between forces and displacements

To offer an explanation of why wall proximity enhances the streamwise vibration amplitude but has little impact on the transverse vibration, the phase angle ϕ_{C_L-Y} between the lift force and the transverse displacement and the phase angle ϕ_{C_D-X} between the drag force and the streamwise displacement have been obtained by Hilbert transform, given in Fig. 6a and b, respectively.

As shown in Fig. 6a, ϕ_{C_L-Y} remains mostly unchanged with the presence of a plane wall in proximity. For both the isolated and the near-wall cases, ϕ_{C_L-Y} is close to 0° (in-phase) in the pre-lock-in and the initial branch of the lock-in regions, and dramatically increases to 180° (out-of-phase) on the lower branch of lock-in with a sudden jump occurring at the demarcation between initial and lower branches. Blackburn and Henderson (1999) and Carberry and Sheridan (2001) pointed out that the phase shift between the lift force and the transverse displacement of the cylinder is associated with a change in the direction of the energy transfer. Based upon this, in Fig. 6a there exists net energy transfer from the fluid to the cylinder in the pre-lock-in and initial branch of the lock-in regions, and vice versa in the lower branch of the lock-in and post-lock-in regions. Here, we can define the energy-in phase as the pre-lock-in and initial branch of the lock-in regions; and the energy-out phase as the lower branch of the lock-in and post-lock-in regions. The positive energy transfer partly leads to the large increase in peak transverse amplitude in the corresponding regimes, shown in Fig. 5a. The sudden jump in phase difference to 180° afterwards, meaning there is no net energy transfer from the fluid to structure, leads to the sudden decrease in peak transverse vibration amplitude, shown in Fig. 5a. It is worth pointing out that at $U_r = 6$ while $\phi_{C_L-Y} = 180^\circ$, meaning the cylinder is damping energy out to the fluid, $(A_y)_{max}/D$ is still relatively large, as shown in Fig. 5a. At $U_r = 6$, it is still inside the lock-in range in which both the vortex shedding frequency and the cylinder vibration frequency lock into the natural frequency of the system. This gives rise to the resonance which leads to large vibration amplitude although work done on the cylinder is negative at this moment. Zhang et al. (2015) pointed out that as U_r increases within the lock-in range, flutter-induced lock-in turns into resonance-induced lock-in across a critical value of U_r . Thus, the root cause of the large vibration amplitude at $U_r = 6$ with $\phi_{C_L-Y} = 180^\circ$ is the resonance-induced frequency lock-in by VIV. That is to say, the large vibration amplitude in the lock-in range is caused by two superimposed factors: frequency lock-in and energy transfer.

As shown in Fig. 6b, ϕ_{C_D-X} has a remarkable difference between the isolated and the near-wall configurations. The difference is noted in the pre-lock-in and the initial branch of the lock-in regions. For the isolated cylinder, ϕ_{C_D-X} is 180° throughout all values of U_r considered. For the near-wall cylinder, the trend of variation of ϕ_{C_D-X} with U_r is very similar to ϕ_{C_L-Y} . Small phase angle (in-phase) is observed in the pre-lock-in and initial branch of lock-in regions, as U_r increases to lower branch, ϕ_{C_D-X} suddenly jumps to 180° . This shows that there exists net energy transfer from the fluid to the structure in the pre-lock-in and initial branch of the lock-in regimes, which largely enhances the streamwise oscillations, as shown in Fig. 5b. In contrast to the near-wall cylinder, ϕ_{C_D-X} for the isolated cylinder remains 180° (out-of-phase), meaning the cylinder is damping energy to the fluid. This leads to the fact that the vibration amplitude is almost negligible for the isolated cylinder on the streamwise direction. From the energy transfer viewpoint, this explains why the wall proximity can largely enhance the streamwise oscillation for an elastically mounted circular cylinder with 2-DoF undergoing VIV. Similar trend of the ϕ_{C_D-X} is also reported in Tham et al. (2015). Similarly with the transverse direction, it is also worth pointing out that

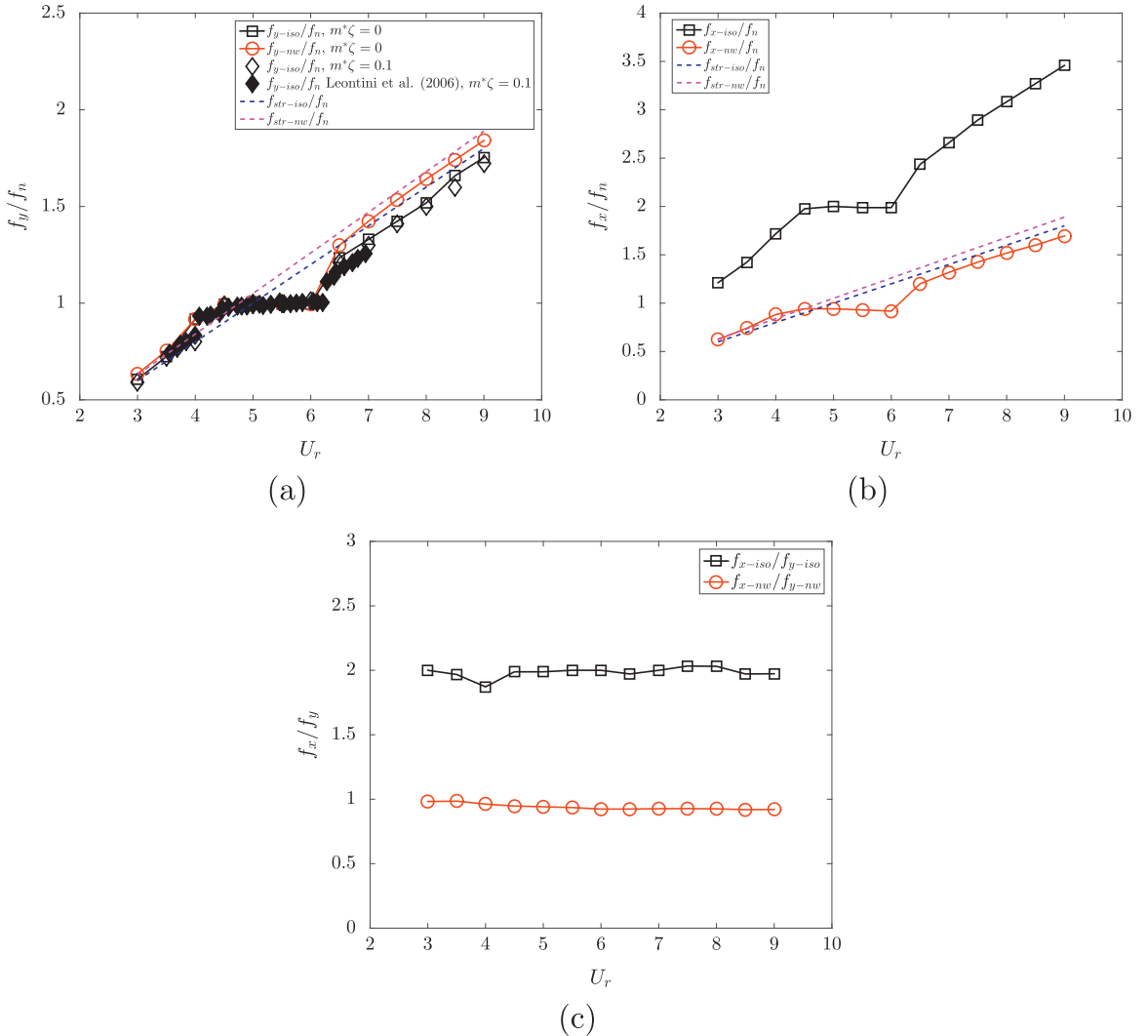


Fig. 7. Response frequencies as a function of reduced velocity U_r for both isolated and near-wall cylinders at $Re=200$: (a) transverse (b) streamwise and (c) ratio of streamwise direction to transverse direction.

though ϕ_{C_D-X} turns into 180° at $5 \leq U_r \leq 6$ for the near-wall cylinder, $(A_x)_{rms}/D$ is still relatively large, as shown in Fig. 5b. The same argument that the frequency lock-in is the root cause of large amplitude vibration and a more predominant factor than energy transfer can also be applied here. The streamwise frequency lock-in observed in the near-wall case is due to the frequency reduction in the streamwise direction, which is initially caused by the suppression of bottom shear layer roll-up. The details of the streamwise frequency lock-in and cylinder-bottom vortex shedding suppression for the near-wall configuration are discussed in Sections 4.4 and 4.6, respectively.

4.4. Response frequencies

In the range of lock-in, the frequency of vortex shedding, f_{vs} , or the frequency of lift force oscillation, f_{G_L} , is in sympathy with the frequency of cylinder vibration, f , according to Williamson and Roshko (1988). They both lock into the natural frequency of the system, f_n , i.e. $f_{vs} \approx f \approx f_n$. The dominant frequencies normalised by the natural frequency f_n as a function of U_r are shown for both the transverse and streamwise directions in Fig. 7a and b, respectively.

A characteristic feature of VIV is that of the lock-in phenomenon, where the vortex shedding frequency diverges from Strouhal's relationship (vortex shedding frequency of a stationary cylinder) and becomes equal or close to the cylinder's natural frequency. The vibration frequency generally increases with reduced velocity U_r . In the transverse direction, shown in Fig. 7a, the response frequencies for an isolated cylinder with mass damping of $m^*\zeta = 0.1$ are first compared with the results from Leontini et al. (2006) to assess the accuracy. For both the isolated and near-wall configurations, the response frequencies behave similarly, following Strouhal's relationship in the pre-lock-in and post-lock-in regions but departing

from Strouhal's relationship and vibrating with the natural frequency in the lock-in region. In the streamwise direction, shown in Fig. 7b, it is evident that the response frequencies of the near-wall cylinder behave very differently from the isolated case. As for the isolated configuration, it is intuitive that the vibration frequency in the streamwise direction is twice of the transverse direction owing to the two alternate vortices shed from the cylinder each cycle. Nonetheless, for the near-wall configuration, the vibration frequency in the streamwise direction does not really differ from that of the transverse direction. This is caused by the fact that the counter-clockwise vortices shed from the bottom surface of the cylinder are suppressed by the wall proximity, as discussed in Section 4.6.

To better identify the difference between the transverse and streamwise directions, the ratios of the response frequencies in the streamwise direction to the transverse direction are plotted for both configurations with the variation of U_r in Fig. 7c. The ratio of the response frequencies in the streamwise direction to the transverse direction for the isolated cylinder is approximately 2, which is consistent with the physics of alternate vortex shedding. However, the ratio becomes unity for the near-wall cylinder. It is observed that in the streamwise direction the vibration frequency of the near-wall cylinder locks into the natural frequency in the lock-in range, whereas the isolated cylinder vibrates with twice the natural frequency. This means that the frequency lock-in is attained in the streamwise direction for the near-wall cylinder, but not for the isolated cylinder. The streamwise frequency lock-in of the near-wall cylinder is the major reason for enlarged streamwise oscillation as compared to the isolated configuration. On top of this, positive energy transfer in the energy-in phase also plays an important role towards enhanced streamwise oscillations.

Therefore, at this point, we may conclude that the wall proximity effects not only strongly enhance the streamwise oscillation but also reduce the streamwise vibration frequency by half. Besides the net energy transfer, the streamwise frequency lock-in is the root cause of higher vibration amplitudes for the vibrating near-wall cylinder than that of the wall-free cylinder. We further investigate what underlying physical mechanism induces the streamwise frequency lock-in.

4.5. Motion trajectories

The XY-trajectory for the isolated cylinder takes the form of a classical figure of eight, as reviewed in Sarpkaya (2004). The trajectories of both isolated and near-wall cylinders are taken from the cylinder displacements during the dimensionless time range $tU/D = 250\text{--}500$. As shown in Figs. 8 and 9, with the presence of a plane wall, the trajectory of the freely vibrating cylinder is changed from the typical figure-eight shape into an oblique elliptical configuration. The shape of an oblique ellipse possessed by the near-wall cylinder is similarly reported by Tsahalis and Jones (1981). This indicates a change in the relative frequency ratio of the transverse and streamwise response, which is consistent with our observation in Fig. 7. The figure-eight shape for the isolated cylinder case is associated with a frequency ratio of $f_y/f_x \approx 2$, while the oblique elliptic trajectory for the near-wall case corresponds to the frequency ratio of $f_y/f_x \approx 1$.

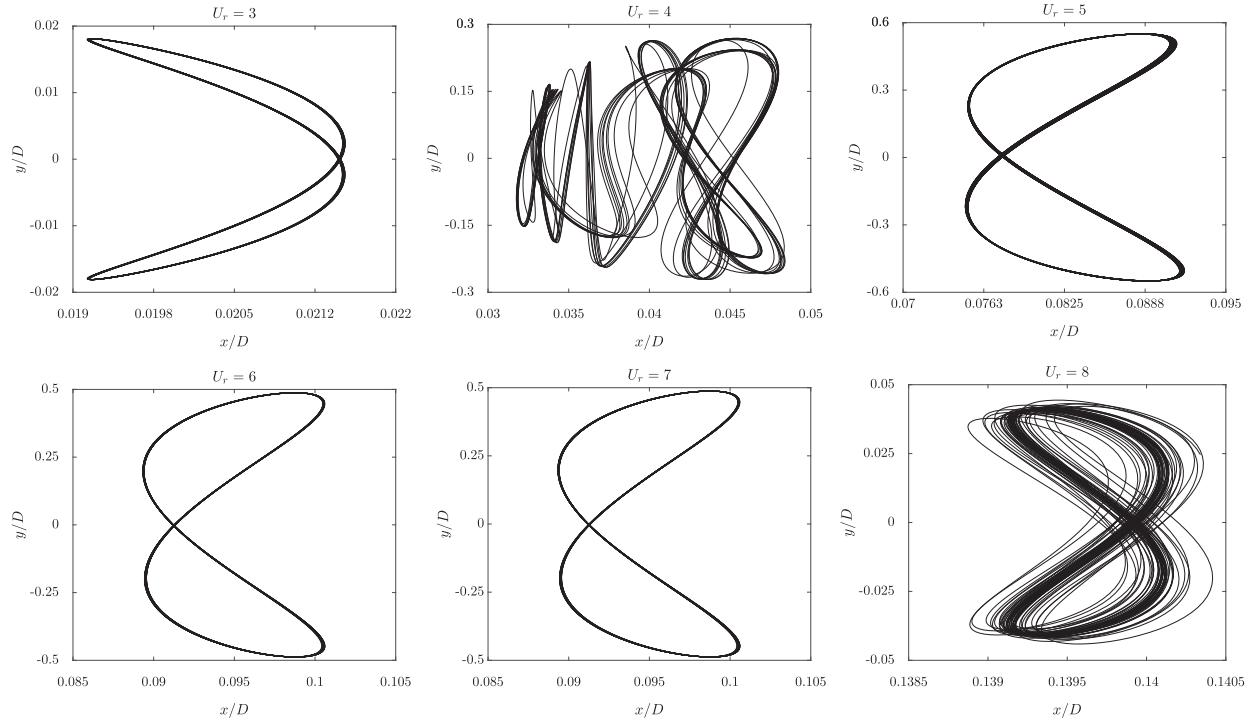


Fig. 8. 2-DoF motion trajectories of isolated cylinder for different reduced velocities U_r at $Re=200$.

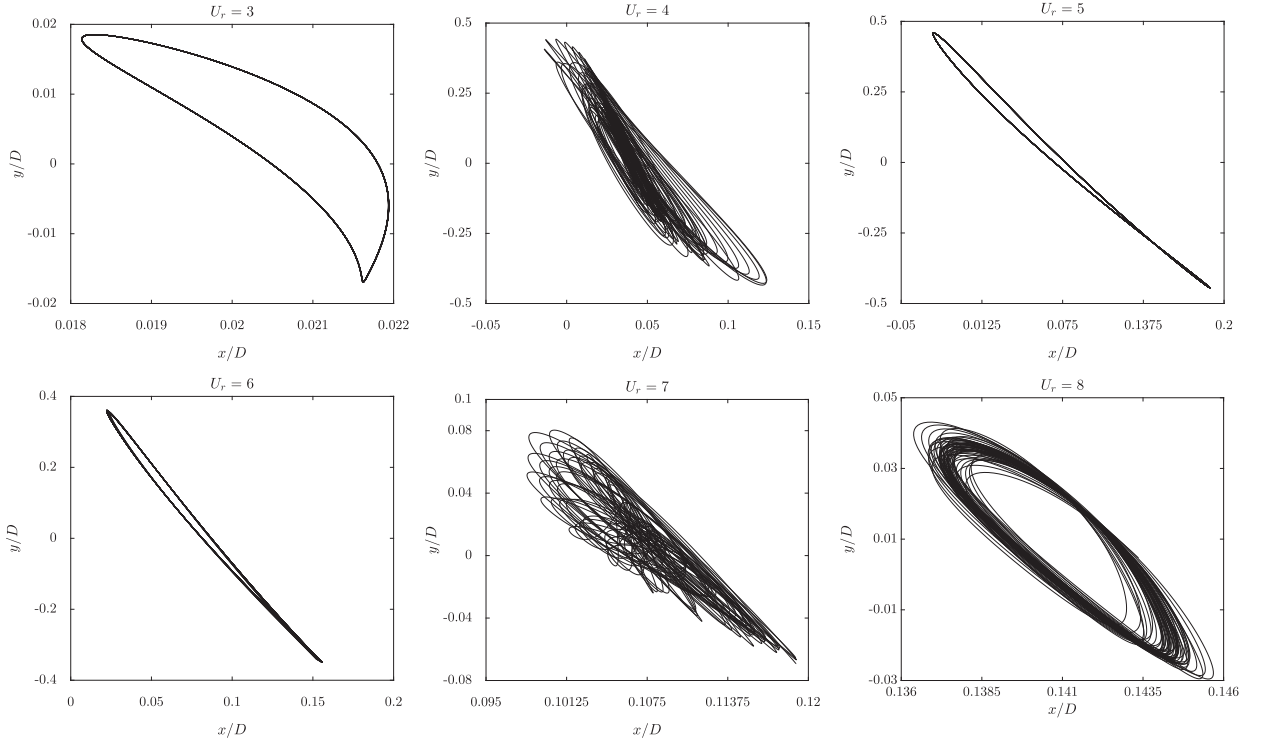


Fig. 9. 2-Dof motion trajectories of near-wall cylinder for different reduced velocities U_r at $Re=200$.

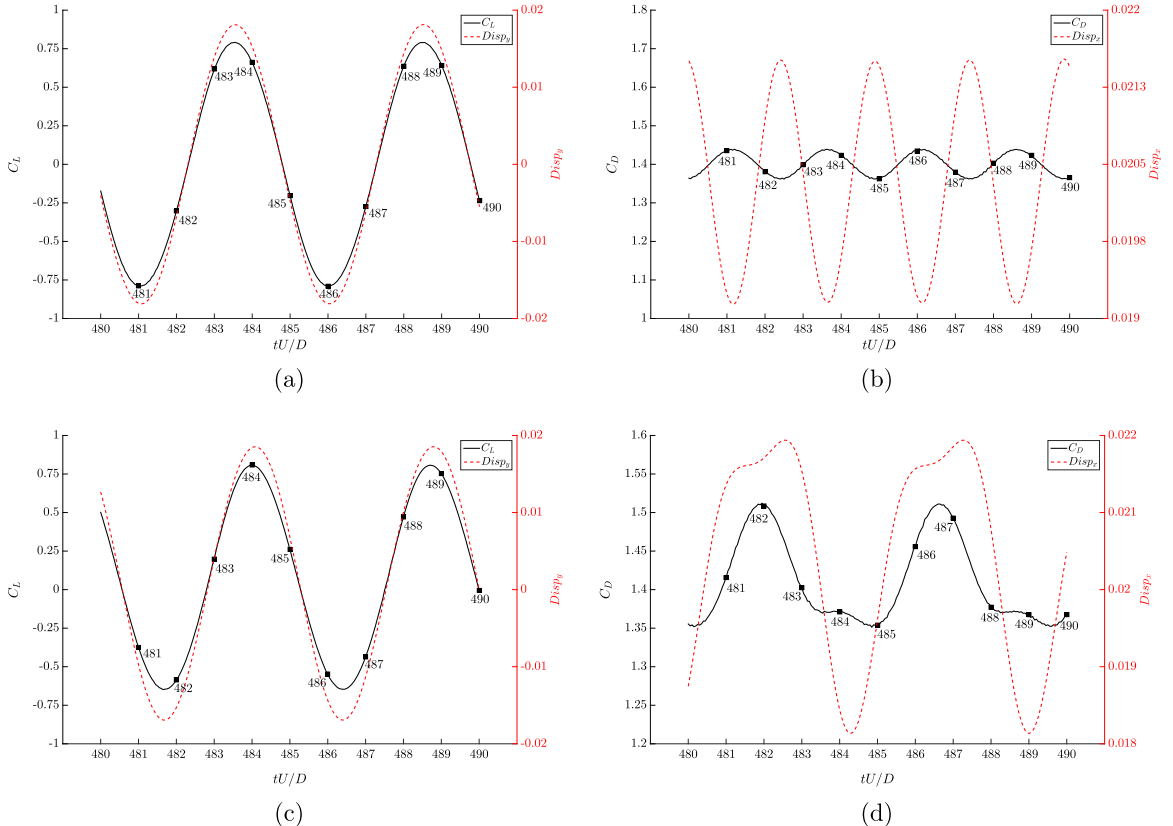


Fig. 10. Selected time histories of (a, c) lift coefficient and transverse displacement (b, d) drag coefficient and streamwise displacement for isolated cylinder (upper) and near-wall cylinder (lower) in pre-lock-in region at $U_r = 3$, $Re = 200$.

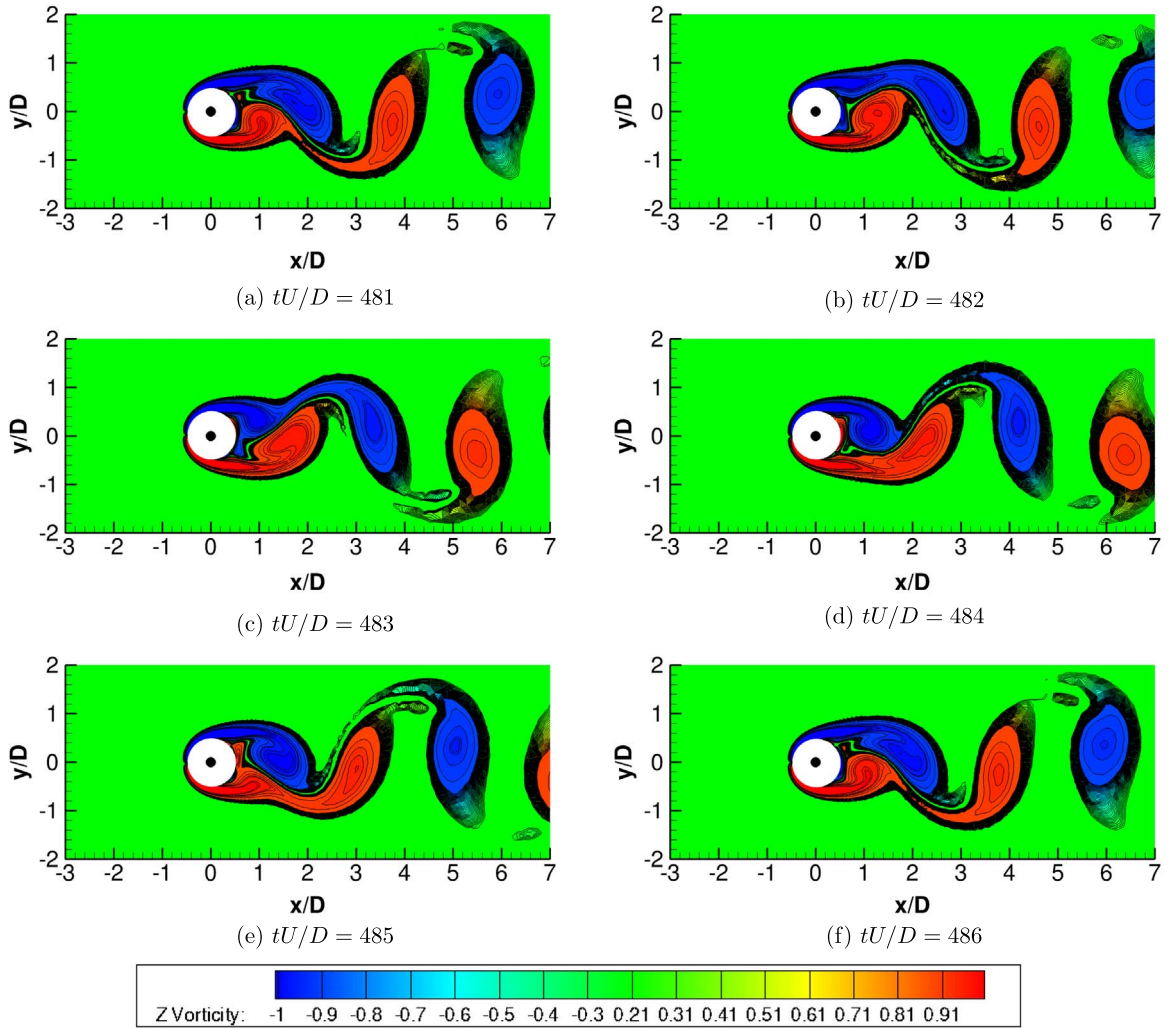


Fig. 11. Vorticity contours for isolated cylinder at $U_r = 3$, $Re = 200$ for discrete time instants from $tU/D = 481$ to 486 for flow coming from left to right. An unsteady 2S wake mode is evident.

One interesting point to note here is that the trajectories at $U_r = 4$ are not as repeatable as what is shown for other reduced velocities. This is because at this particular reduced velocity, VIV undergoes a transition from the pre-lock-in to the lock-in regime, thus the cylinder responses become increasingly sensitive to the change in reduced velocity. As Zhang et al. (2015) pointed out, the cylinder vibration mode transitions from the wake mode (weak interaction) to a combined wake and structure mode (strong interaction) across the critical value of U_r between the pre-lock-in and lock-in. This mode switching gives rise to the unstable and non-repetitive trajectories. Details and explanations of this phenomenon are given in Section 4.8.

4.6. Flow fields

In this section, we investigate the flow field and vortices associated with the VIV of the cylinder for both isolated and near-wall configurations. We select three representative reduced velocities, $U_r = 3, 5$ and 8 , in the pre-lock-in, lock-in and post-lock-in regions, respectively. To investigate how the wall proximity affects the vortex dynamics, we look into the time histories of the force coefficients and cylinder displacements at some specific time steps and connect them with the corresponding vorticity contours. The detailed mechanism for vortex shedding suppression of bottom shear layer roll-up is also described in the following subsections.

4.6.1. Pre-lock-in region at reduced velocity $U_r = 3$

As shown in Fig. 10, for the isolated cylinder, the transverse force and vibration are in-phase (Fig. 10a) but the force and amplitude are out-of-phase in the streamwise direction (Fig. 10b). For the near-wall cylinder, the hydrodynamic force and

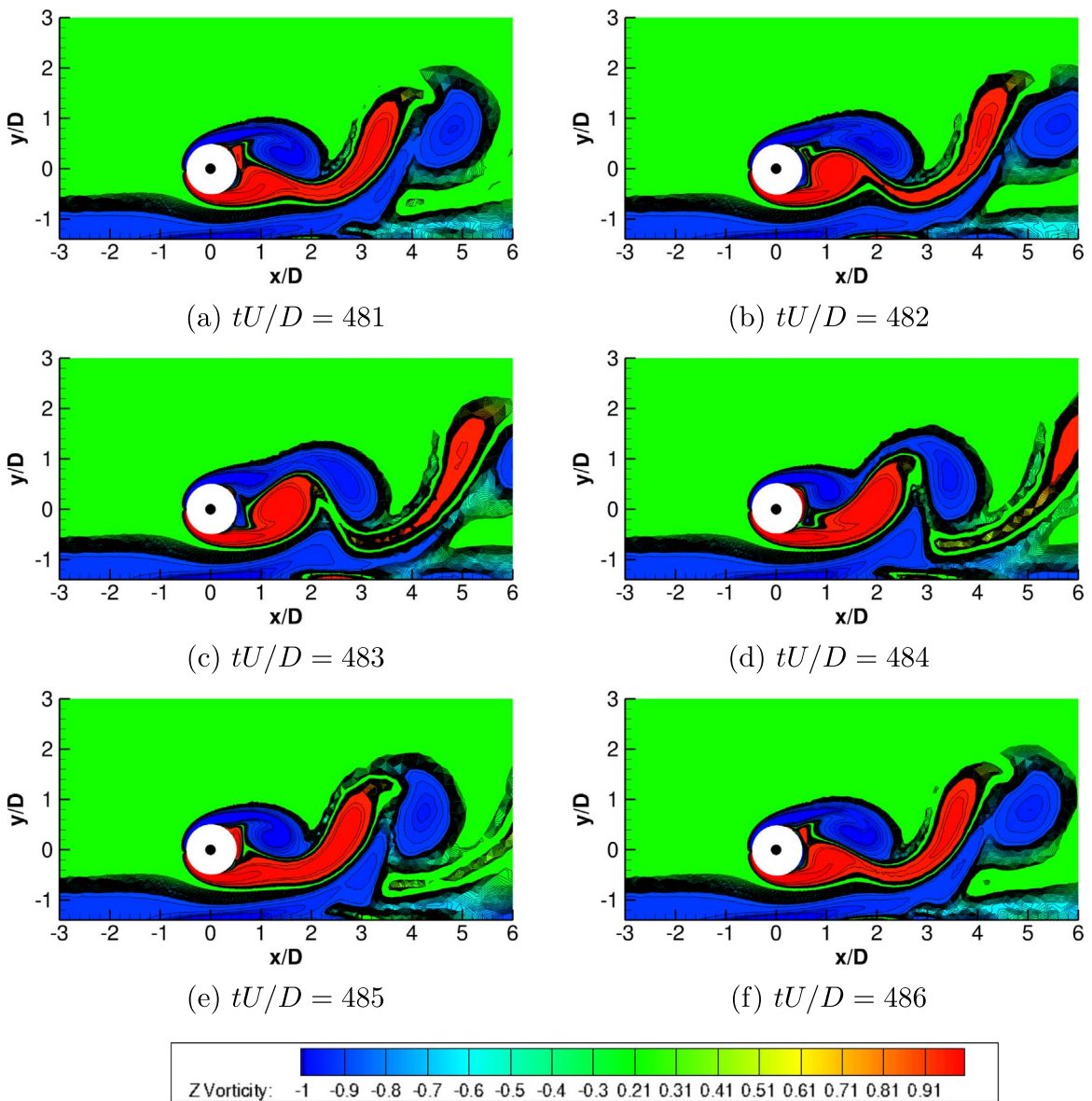


Fig. 12. Vorticity contours for near-wall cylinder at $U_r = 3$, $Re = 200$ for discrete time instants from $tU/D = 481$ to 486 for flow coming from left to right. Coalescing of clockwise vortex with wall boundary layer can be seen.

the vibration amplitude are in-phase for both transverse and streamwise directions. This is consistent with what we have observed in Fig. 6. The phase difference between the lift force and the transverse displacement is approximately 0° for both isolated and near-wall cylinders and the phase differences between drag and streamwise displacement are 180° and 0° for the isolated and near-wall cylinders, respectively.

The corresponding vorticity contours are presented in Figs. 11 and 12. The black dot marked in the plot represents the initial location of the cylinder as a reference. At $U_r = 3$, the displacements in both transverse and streamwise directions are negligible since it is still in the pre-lock-in region. In Fig. 11, regular alternate vortices are shed from the cylinder undergoing VIV, clockwise (negative) vortices from the upper surface and counter-clockwise (positive) from the lower surface of the cylinder. In Fig. 12, the clockwise vortices shed from the upper surface of the cylinder coalesce with the clockwise wall boundary layer vortices. This coalescing action strengthens the negative vortices, suppressing the positive ones shed from the lower surface of the cylinder.

To better illustrate this mechanism of the bottom shear layer roll-up suppression in the near-wall configuration, a schematic diagram is presented in Fig. 13. The wall boundary layer is forced to separate by the counter-clockwise Vortex B shed from the bottom surface of the cylinder. The counter-clockwise Vortex B induces an upward velocity onto the separated wall boundary layer, producing a secondary clockwise Vortex C from the wall vorticity layer which eventually merges

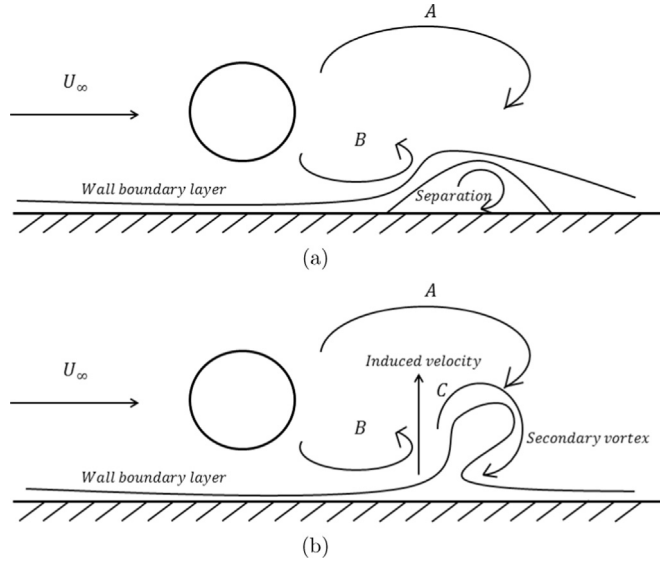


Fig. 13. An illustration for interaction of vortices shed from the near-wall cylinder with the wall boundary layer.

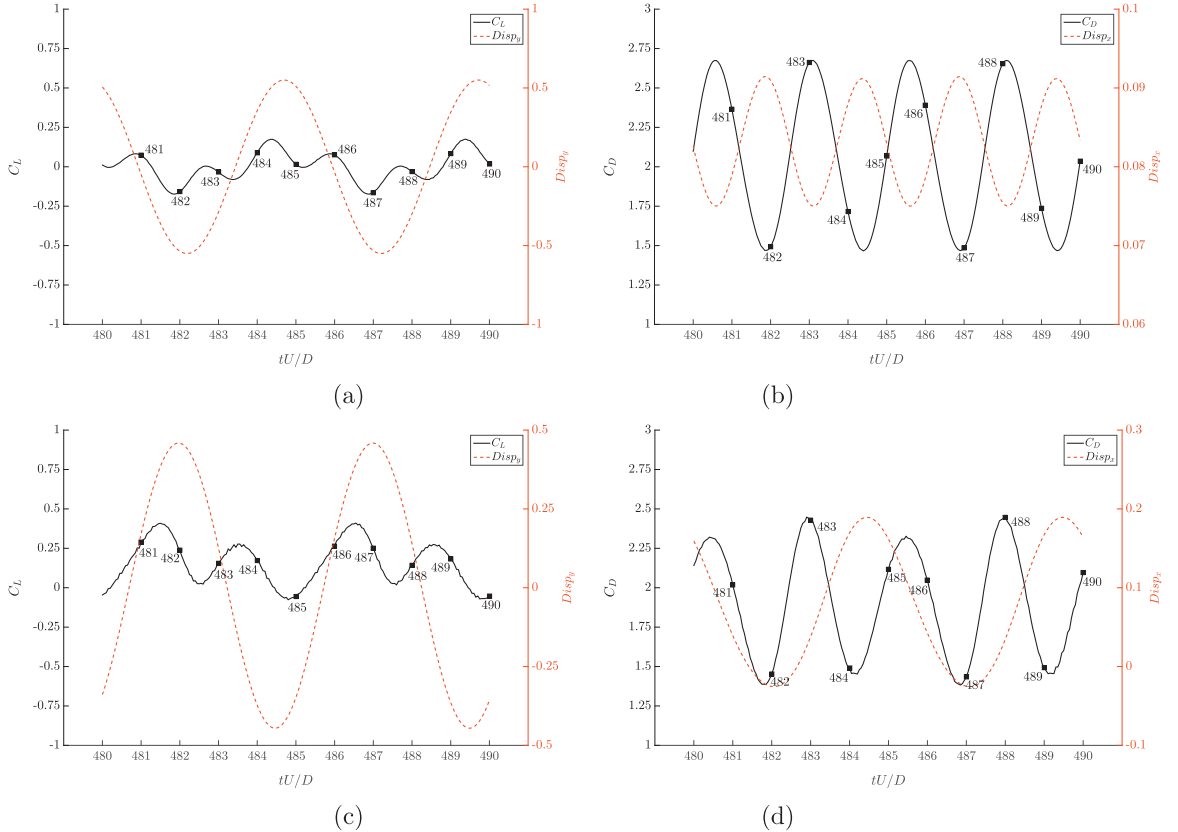


Fig. 14. Selected time histories of (a, c) lift coefficient and transverse displacement (b, d) drag coefficient and streamwise displacement for isolated cylinder (upper) and near-wall cylinder (lower) in lock-in region at $U_r = 5$, $Re = 200$.

with the clockwise Vortex A shed from the upper surface of the cylinder. The coalescence of Vortex A and Vortex C in turn suppresses counter-clockwise Vortex B. A similar mechanism for the interaction of wake vortices with ground effects was summarised by Puel and Victor (2000). The suppression of the counter-clockwise vortices shed from the bottom of the cylinder is the reason why the ratio of streamwise vibration frequency to transverse vibration frequency becomes unity rather than 2, which leads to streamwise frequency lock-in and eventually the enhanced streamwise oscillations.

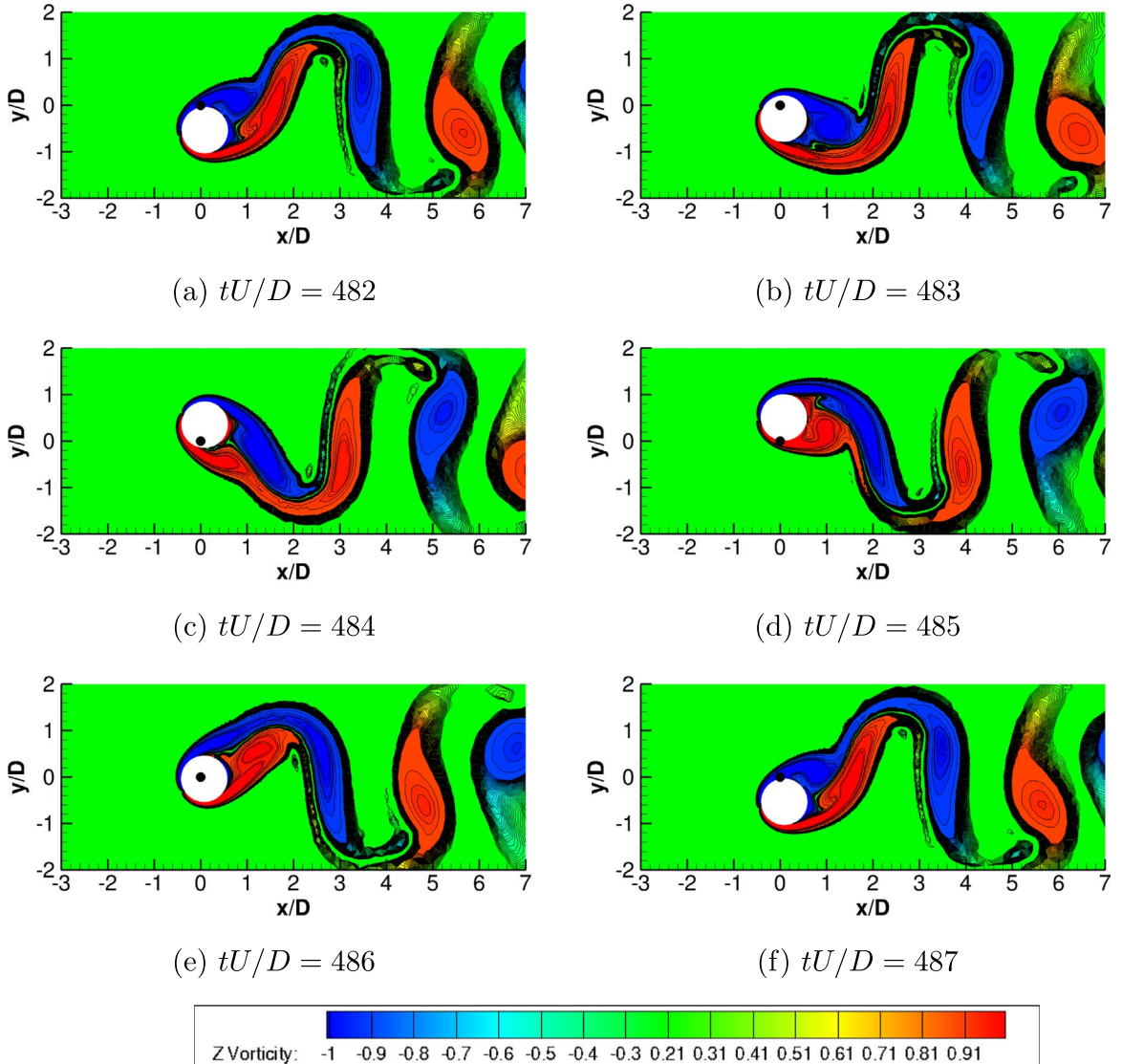


Fig. 15. Vorticity contours for isolated cylinder at $U_r = 5$, $Re = 200$ for discrete time instants from $tU/D = 482$ to 487 for flow coming from left to right. Stretching of vortices can be seen due to large amplitude motion.

4.6.2. Lock-in region at reduced velocity $U_r = 5$

At $U_r = 5$, the cylinder undergoes VIV in the synchronization regime whereby the large vibration amplitudes are expected. The time traces of the force coefficients and displacements for both isolated and near-wall cylinders at $U_r = 5$ at some specific time steps are illustrated in Fig. 14. A relatively small lift force and large transverse displacement can be observed for both the configurations. However, large streamwise displacement can be found for the near-wall cylinder in comparison to the isolated counterpart whereas the drag force of the two configuration is quite similar.

The corresponding vorticity contours are presented in Figs. 15 and 16. To analyse the relation between the vortices shed from the cylinder and the force acting on the cylinder, as shown in Fig. 14c, the movement of near-wall cylinder is considered from its most negative to the most positive displacement from $tU/D = 485$ to 487 . At $tU/D = 485$, a strong clockwise vortex starts to form on the upper surface of the cylinder, and this vortex is rolling in clockwise from $tU/D = 485$ to 487 and exerting a large upward force vertically onto the cylinder. The clockwise vortices shed from the upper surface of the cylinder coalesce with the clockwise vorticity layer over the wall. This coalescing phenomenon strongly strengthens the negative vortices, suppressing the positive ones shed from the lower surface of the cylinder. This mechanism of cylinder bottom vortex suppression is much more pronounced in the lock-in region at $U_r = 5$ as compared to the pre-lock-in region at $U_r = 3$. Also shown in Fig. 15, the vortices shed from the cylinder are much wider in the transverse direction than those for $U_r = 3$ (see Fig. 11) owing to the larger vibration amplitude.

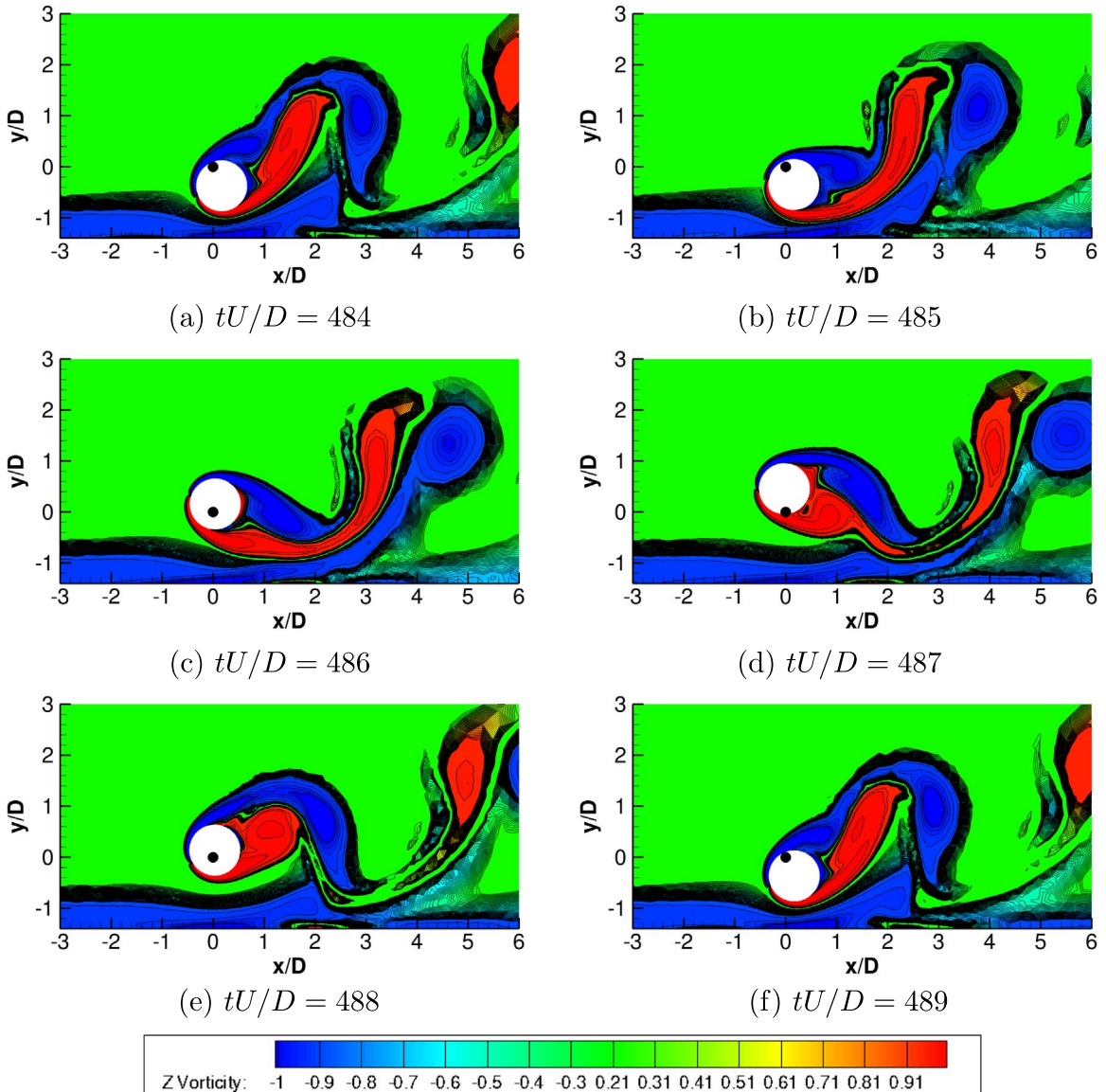


Fig. 16. Vorticity contours for near-wall cylinder at $U_r = 5$, $Re = 200$ for discrete time instants from $tU/D = 484$ to 489 for flow coming from left to right. Stronger coalescing phenomenon strengthens the negative vortices while suppressing the positive ones shed from the lower surface of the cylinder.

4.6.3. Post-lock-in region at reduced velocity $U_r = 8$

At $U_r = 8$, the cylinder undergoes VIV in the post-lock-in range, where the hydrodynamic force and the displacement are out-of-phase in both transverse and streamwise directions for both isolated and near-wall cylinders, observed in Fig. 17. The time traces of the lift coefficient and displacement exhibit harmonic behaviour for both configurations. This is also consistent with the observation from Fig. 6. The flow field in the post-lock-in region, shown in Figs. 18 and 19, looks similar to that of at $U_r = 3$ in the pre-lock-in region.

4.7. Vortex shedding modes

The instantaneous vorticity fields for the fully developed flow for both isolated and near-wall cylinders undergoing VIV at four selected reduced velocities of $U_r = 3, 4, 5$ and 8 are illustrated in Fig. 20. The “2S” and “C(2S)” vortex shedding modes are described in Williamson and Roshko (1988) and similarly reported in the literature of laminar VIV of isolated cylinder such as Singh and Mittal (2005), Zhou et al. (2012) and Tang et al. (2013). At low Reynolds number, in the laminar regime, (Singh and Mittal, 2005) found that the mode of vortex shedding is primarily “2S”, but “C(2S)” is observed when the cylinder undergoes high-amplitude oscillations. They also reported the existence of a “P+S” mode of vortex shedding at $Re \geq 300$ (Govardhan and Williamson, 2000) and (Khalak and Williamson, 1999) reported the “2S” mode of shedding for the initial

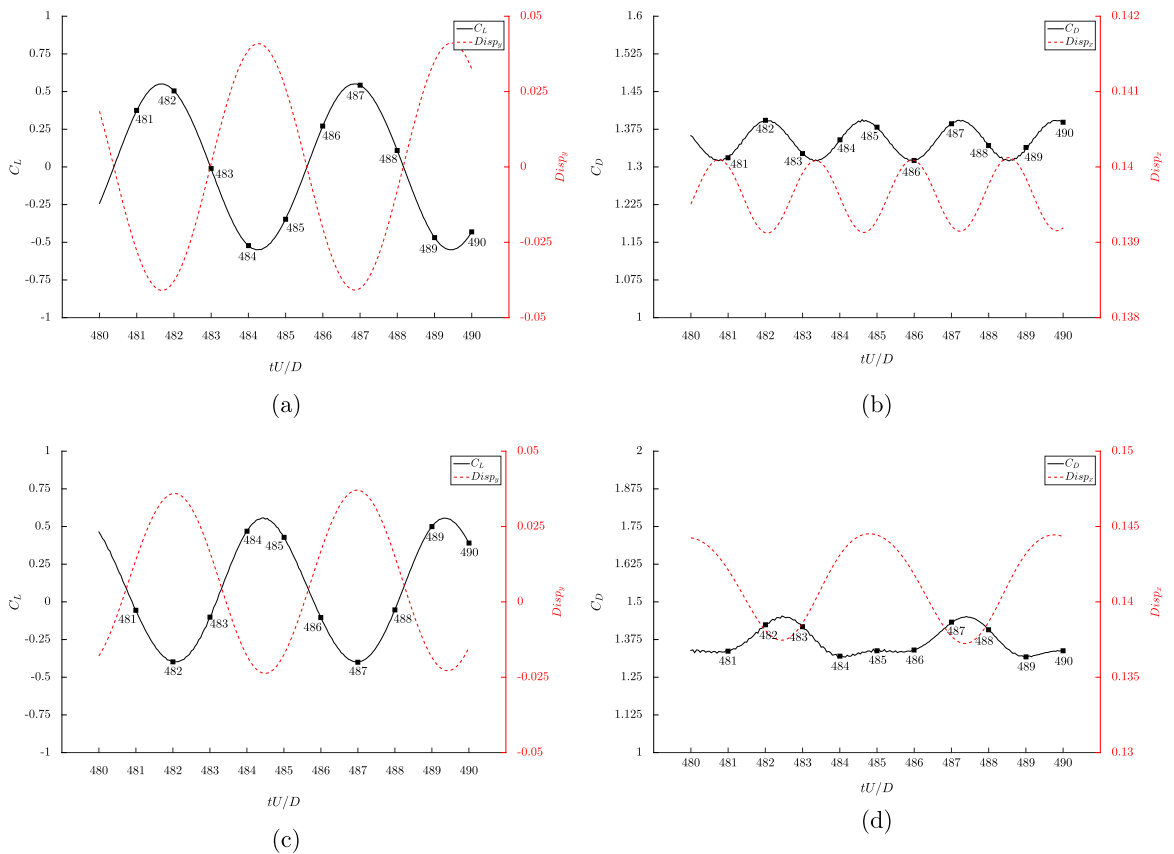


Fig. 17. Selected time histories of (a, c) lift coefficient and transverse displacement (b, d) drag coefficient and streamwise displacement for isolated cylinder (upper) and near-wall cylinder (lower) in post-lock-in region at $U_r = 8$, $Re = 200$.

branch and “2P” mode of shedding in the upper and lower branches.

For the isolated cylinder, the vortex shedding possesses a “2S” mode for all reduced velocities considered, shown in the left column of Fig. 20. To be more specific, as U_r increases from 3 to 5, the separation distance between the positive and negative vortex rows becomes increasingly larger as VIV transforms from the pre-lock-in to the lock-in state. For the values of U_r where the cylinder executes high-amplitude transverse vibration, e.g. $U_r = 5$, the vortex shedding develops into two parallel rows. The distance between the parallel rows is larger than that of $U_r = 4$ owing to the larger displacement in the lock-in region. When $U_r = 8$ in the post-lock-in region, the “2S” mode recovers to what is shown for the pre-lock-in region at $U_r = 3$.

When the cylinder is placed in proximity to a plane wall, some drastic changes occur in the flow around the cylinder, the break-down of symmetry in the flow and the suppression of bottom shear layer roll-up in general, shown in the right column of Fig. 20. The suppression of bottom vortex shedding is closely connected with the asymmetry in the development of the vortices on both sides of the cylinder. The shear layer on the wall-side of the cylinder will not develop as strongly as the shear layer on the freestream side. The combined VIV and wall-induced oscillations due to the asymmetric wake dynamics has also been reported in Sumer and Fredsøe (2006). Vortex shedding mode “1S” is observed at $U_r = 3$ and 4, in which the positive vortices are strongly suppressed due to the presence of the plane wall since almost no positive vortices can be seen in the downstream. As U_r increases to 5, weak “2S” mode can be seen, where weakly developed positive vortices can be observed in the downstream but become weaker as it goes to downstream due to the wall proximity effects which suppress the development of positive vortices on the lower surface of the circular cylinder. When $U_r = 8$, the “1S” mode recovers to what is shown for $U_r = 3$ as it transfers to the post-lock-in region. The suppression of counter-clockwise vortices or the shedding of mere clockwise vorticity from the upper surface of the cylinder leads to the earlier observation that the ratio of streamwise vibration frequency to transverse vibration frequency becomes unity when the cylinder is placed in the vicinity of a plane wall.

4.8. Beating phenomenon

The beating oscillations are described in this section for two selected reduced velocities of $U_r = 4$ and 6.5, which correspond to the critical values for VIV enters and leaves the lock-in range, respectively. In previous studies, Leontini et al.

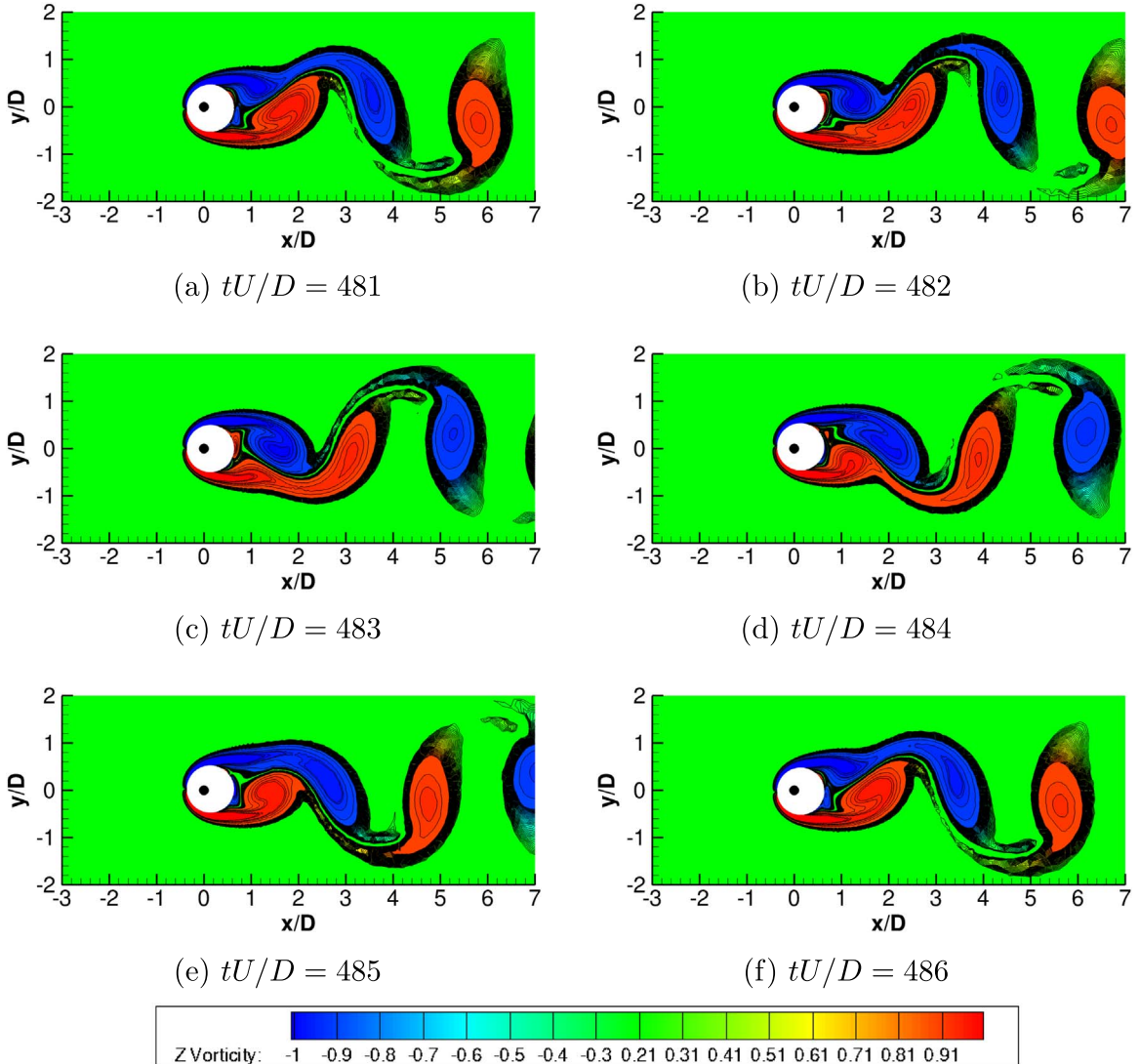


Fig. 18. Vorticity contours for isolated cylinder at $U_r = 8$, $Re = 200$ for discrete time instants from $tU/D = 481$ to 486 for flow coming from left to right. A standard 2S wake mode can be seen.

(2006) reported the intermittent responses of the cylinder at $U_r = 4.6$, whereas Prasanth and Mittal (2008) described the intermittent regime and the mode switching during the transition from the initial to the lower branch. The intermittent regime of the upper-lower branch transition for $4.7 < U_r < 4.8$ is reported in Navrose and Mittal (2013).

4.8.1. Time histories of $U_r = 4$ and 6.5

The traces of lift force and transverse displacement as well as the drag force and streamwise displacement with respect to $U_r = 4$, the critical U_r at which VIV enters the lock-in range, for both isolated and near-wall cylinders are displayed in Fig. 21. It is evident that both the hydrodynamic force and the displacement on both transverse and streamwise directions clearly exhibit beating oscillations. This kind of beating phenomenon has been reported in Leontini et al. (2006). As for the isolated cylinder, shown in Fig. 21a and b, long-period oscillations are evident in both forces and cylinder amplitudes, giving rise to the classification of this case as weakly chaotic, as found in Blackburn and Henderson (1999) for forced cylinder motion in transverse direction.

Notably we observe that when the cylinder is brought close to the plane wall, the absence of periodical repetition, which is clearly observed for the isolated case, reveals the characteristic of random oscillation, as shown in Fig. 21c and d. Particularly in the streamwise direction, the drag force and cylinder displacement exhibit non-periodic and chaotic beating patterns with variable amplitudes and frequencies. This brings the need to utilise Hilbert–Huang transform to conduct the frequency analysis in the following subsection. It can be inferred here that the wall proximity breaks up the periodicity of the time histories of force and displacement presented by the isolated cylinder. Further, comparing Fig. 21c and d, the

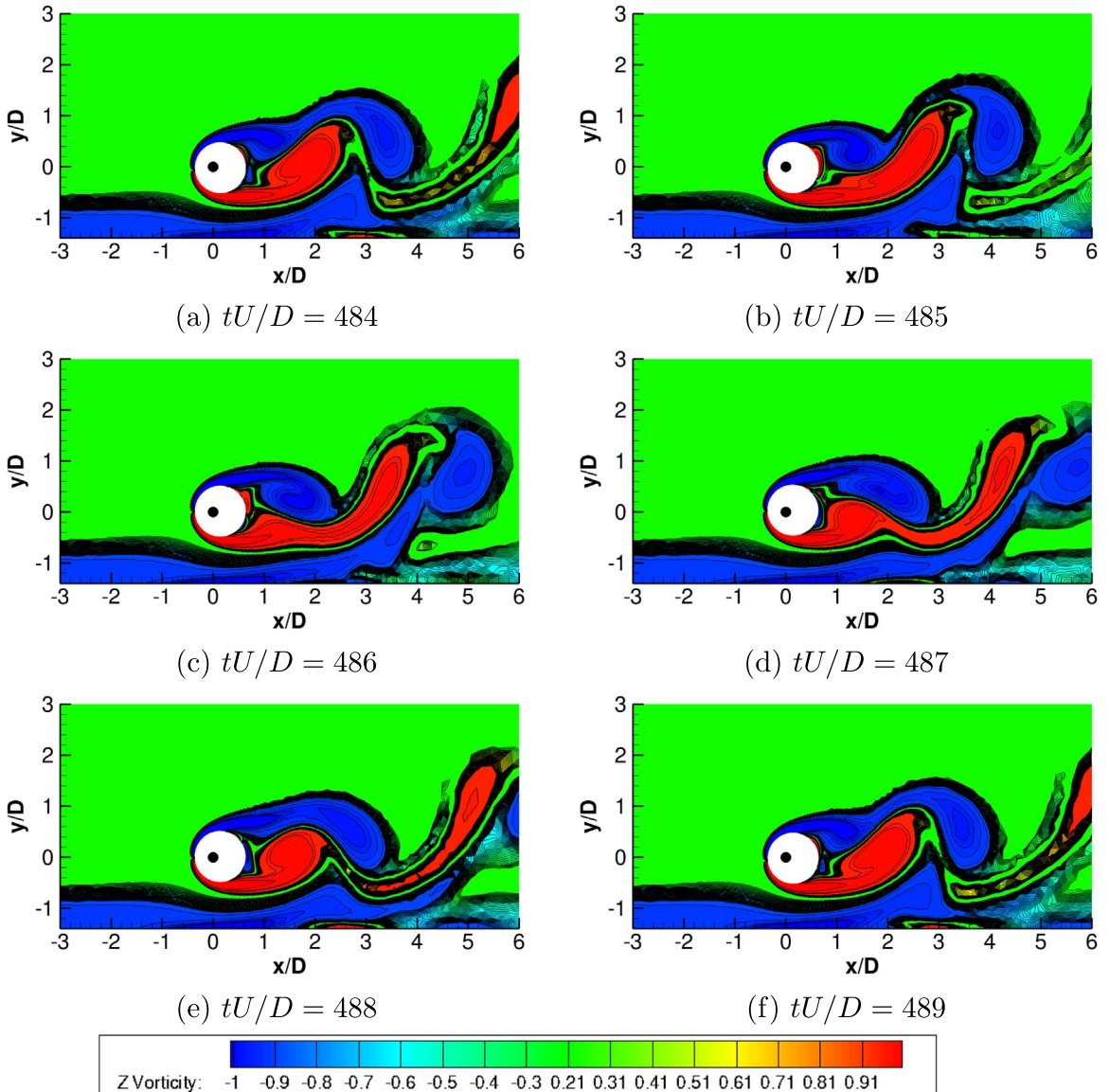


Fig. 19. Vorticity contours for near-wall cylinder at $U_r = 8$, $Re = 200$ for discrete time instants from $tU/D = 484$ to 489 for flow coming from left to right. Merging of wall vorticity layer with clockwise vortices from top cylinder surface can be seen.

beating oscillation in force is much more sensitive in the streamwise direction than the transverse direction.

The traces of lift force and transverse displacement as well as the drag force and streamwise displacement with respect to $U_r = 6.5$, the critical U_r at which VIV leaves the lock-in range, for both isolated and near-wall cylinders are displayed in Fig. 22. Beating oscillation can still be clearly observed for lift force acting on the isolated cylinder, shown in Fig. 22a. When the cylinder is put close to the wall, illustrated by Fig. 22c and d, the non-periodicity of force and displacement does not clearly occur due to the wall proximity, as compared to $U_r = 4$ discussed above. This shows that the hydrodynamic forces and the cylinder responses are more sensitive to the wall proximity when entering the lock-in range than leaving the lock-in range. This can be further deduced to the conclusion that the cylinder at energy-in phase (at $U_r = 4$) is more sensitive to the wall proximity than the cylinder at energy-out phase (at $U_r = 6.5$).

4.8.2. Analysis by Hilbert–Huang transform

To further analyse the beating oscillations observed above, we employ Hilbert–Huang Transform (HHT) (Huang and Wu, 2008) for determining the dominant and sub-dominant frequencies during VIV process. Compared to standard Fast Fourier Transform (FFT), HHT allows us to diagnose time-varying signal with variable amplitudes and frequencies. In this study, for the near-wall configuration the wall proximity causes a nearly random switching, as shown in Fig. 21c and d, in which frequency and amplitude of fluid variables are changing over time. FFT is not able to analyse these signals whereby HHT can

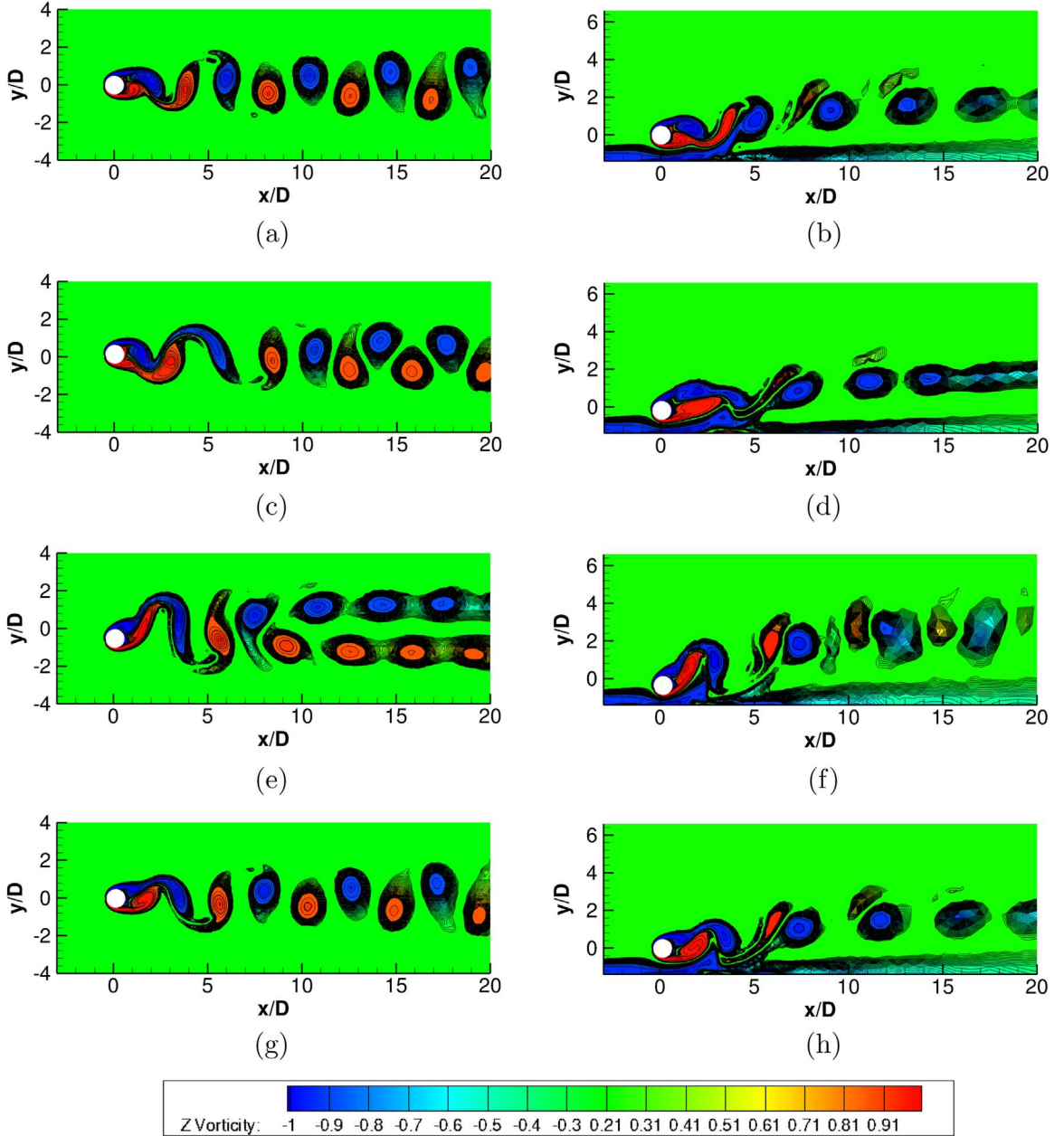


Fig. 20. Vortex shedding modes at (a, b) $U_r = 3$ (c, d) $U_r = 4$ (e, f) $U_r = 5$ (g, h) $U_r = 8$ at $Re=200$ for isolated (left) and near-wall (right) cylinders.

decompose the signals and reveal their instantaneous information (e.g. instantaneous amplitude and frequency) regardless of the time-variant characteristics of original signal.

HHT consists of two primary analytical techniques. Empirical Mode Decomposition (EMD) decomposes the original signal into different modes, so-called intrinsic mode functions (IMF), through a recursive subtraction process of IMFs from the original signal, so-called sifting process. This sifting process is governed by a standard deviation. These resultant IMFs are time-variant (instantaneous frequency and amplitude which are not constant with respect to time) signals and each IMF characterizes not only a narrow band with one mode of oscillation but also both amplitude and frequency modulations. Following EMD, these IMFs are processed by Hilbert Transform (HT) which converts a real signal into its corresponding analytical signal. These intrinsic mode functions in EMD are prepared for HT analysis to return the accurate information of the signal. The basic steps of HHT can be outlined as follows:

- (1) Identify local extrema and link them to form an envelope which are spline fitted.
- (2) Find the mean values among each pair of local maximum and minimum, which are connected to form a signal and

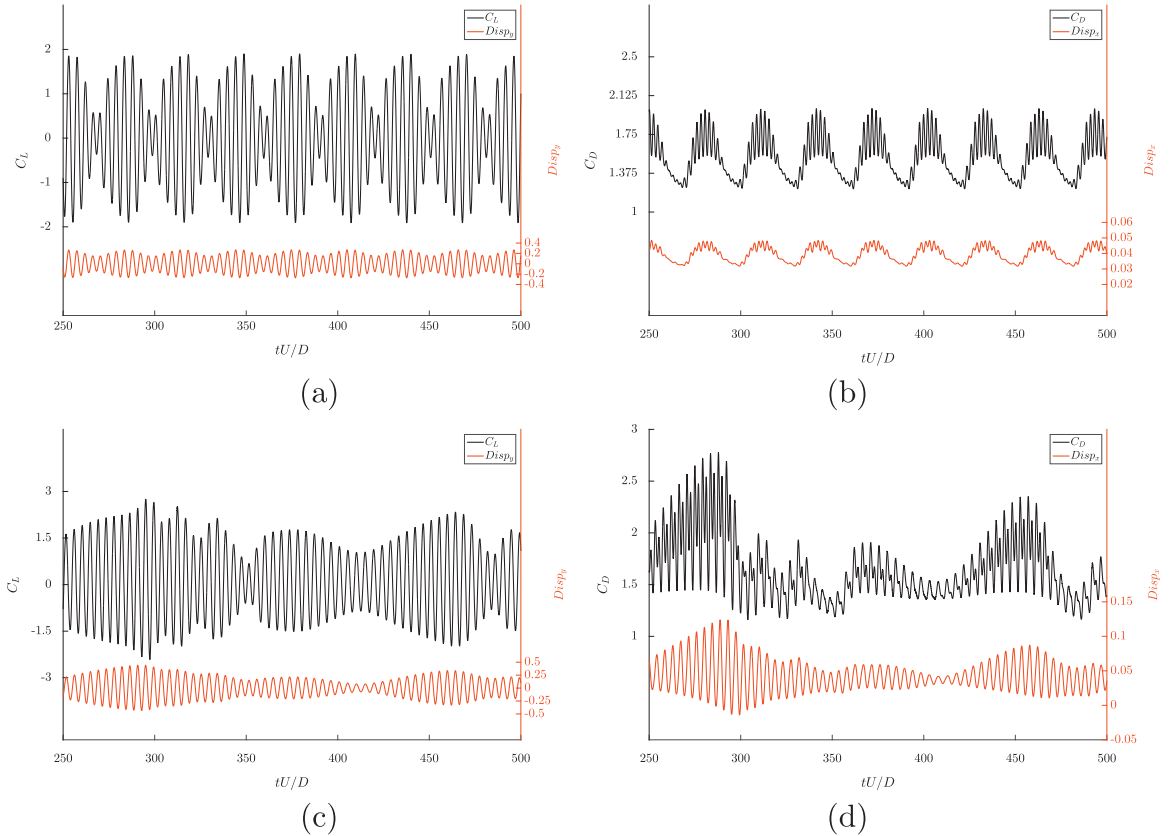


Fig. 21. Time traces of (a, c) lift coefficient and transverse displacement (b, d) drag coefficient and streamwise displacement for isolated (upper) and near-wall (lower) cylinders from $tU/D = 250$ to 500 at $U_r = 4$, $Re = 200$.

subtracted from the original signal, then repeat this step until the mean-value formed signal satisfies the definition of IMF.

- (3) Define this signal as IMF and subtract it from the original signal and repeat step (ii) to find the rest of the IMFs.
- (4) Implement Hilbert Transformation on each IMF to explore the temporal information of the original signal as

$$Z_i(t) = A_i(t) + jB_i(t) = M_i(t)e^{j\phi_i(t)} \quad (13)$$

where $M_i(t)$ and $\phi_i(t)$ are the amplitude and phase angle of each IMF mode, respectively. $A_i(t)$ and $B_i(t)$ denote the i th IMF and its corresponding Hilbert Transform, respectively, the term $B_i(t)$ is given by

$$B_i(t) = \frac{1}{\pi} Q \int_{-\infty}^{\infty} \frac{A_i(\tau)}{t - \tau} d\tau \quad (14)$$

where Q is the Cauchy principal value of the singular integral.

- (5) Having obtained the IMF components, the instantaneous frequency can be computed using the Hilbert Transform in the following form:

$$X(t) = \text{Real} \left[\sum_{i=1}^n M_i(t) e^{j \int \omega_i(t) dt} \right] \quad (15)$$

where $\omega_i(t) = \frac{d}{dt}[\phi_i(t)]$ is the angular frequency.

The Hilbert–Huang spectra for the responses of both isolated and near-wall cylinders at $U_r = 4$ and $U_r = 6.5$ are presented in Figs. 23 and 24, respectively. The y -axis denotes the dimensionless Strouhal frequency and the colourbar is the magnitude or modulus of $Z_i(t)$ (dimensionless since the inputs, displacement and time, are both dimensionless), given in Eq. (13). In this case, the intensity of the colour in the plots can be understood as a measure of the vibration amplitude at the given frequency. In Fig. 23, in the transverse direction, the presence of the wall does not alter the dominant frequency which is approximately 0.2, by comparing Fig. 23a and c. However, via comparing Fig. 23b and d, in the streamwise direction, the wall in proximity reduces the higher frequency band while the lower frequency band remains almost unchanged. We can

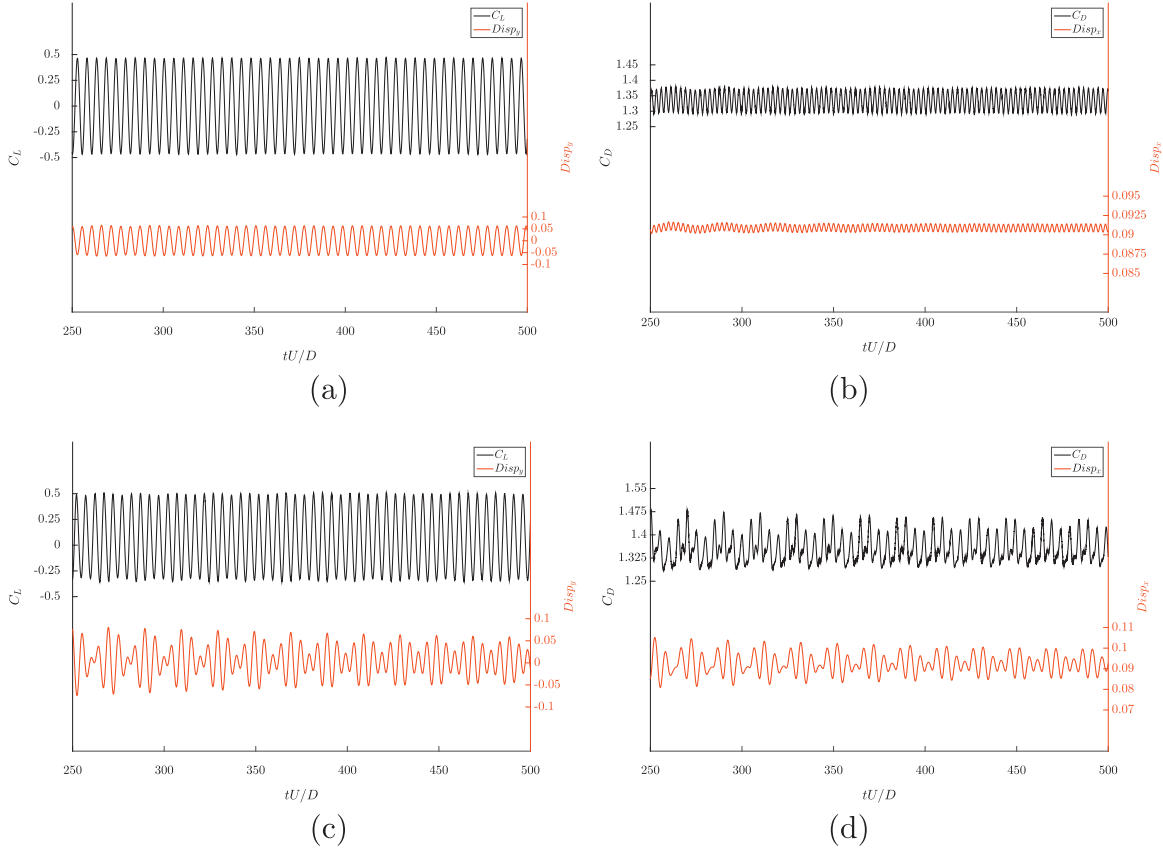


Fig. 22. Time traces of (a, c) lift coefficient and transverse displacement (b, d) drag coefficient and streamwise displacement for isolated (upper) and near-wall (lower) cylinders from $tU/D = 250$ to 500 at $U_r = 6.5$, $Re = 200$.

reaffirm that, due to the presence of the wall, the beating oscillation is more sensitive in the streamwise direction than the transverse direction. In Fig. 24, on the other hand, at $U_r = 6.5$ the critical point of leaving the lock-in region, the wall proximity induces multiple components of frequency on both directions, in comparison with single component of frequencies presented in the isolated cylinder. In the streamwise direction, the dominant frequency is reduced by half (i.e., period doubling), which is consistent with the earlier findings. This HHT analysis shows that the wall proximity affects the response frequencies differently for both energy-in and energy-out phases.

5. Three-dimensional results and discussion

Our discussion of the VIV dynamics of a circular cylinder with 2-DoF has thus far been based upon a key assumption that for $Re=200$ the underlying flow phenomena can be adequately described by 2D simulations. The flow around an isolated cylinder, however, has been shown to transit to 3D at $Re=188$, according to Karniadakis and Triantafyllou (1992). Nonetheless, $Re=200$ is widely considered in the literature to be the upper threshold for which the wake flow remains 2D, and such examples are Tham et al. (2015), Carmo and Meneghini (2006, 2007) and Papaioannou et al. (2006). Thus, such 2D simulations for $Re=200$ presented in the previous section should be appropriate. To fully examine the wall proximity effects on VIV of an elastically mounted circular cylinder with 2-DoF, we perform 3D simulations by considering circular cylinders of finite span in both isolated and near-wall configurations.

VIV of an elastically mounted circular cylinder with 2-DoF at $Re=1000$, the beginning of the subcritical regime, in 3D is simulated for U_r ranging from 3 to 9 with an interval of 1. In order to capture long and short timescale variations in the fluid flow, at least 50 periodic variations of the cylinder vibration are simulated till the dimensionless time $tU/D = 250$ with a time step size of $\Delta t = 0.05$ in the present 3D studies. For the purpose of direct comparison, 2D VIV simulations are also conducted at $Re=1000$ for both configurations, and the 2D results are presented together with the 3D results in the following cylinder responses and the hydrodynamic force coefficients' plots. We show the invalidity of 2D numerical simulations for VIV in the subcritical regime in terms of the computations for the cylinder responses and hydrodynamic force coefficients.

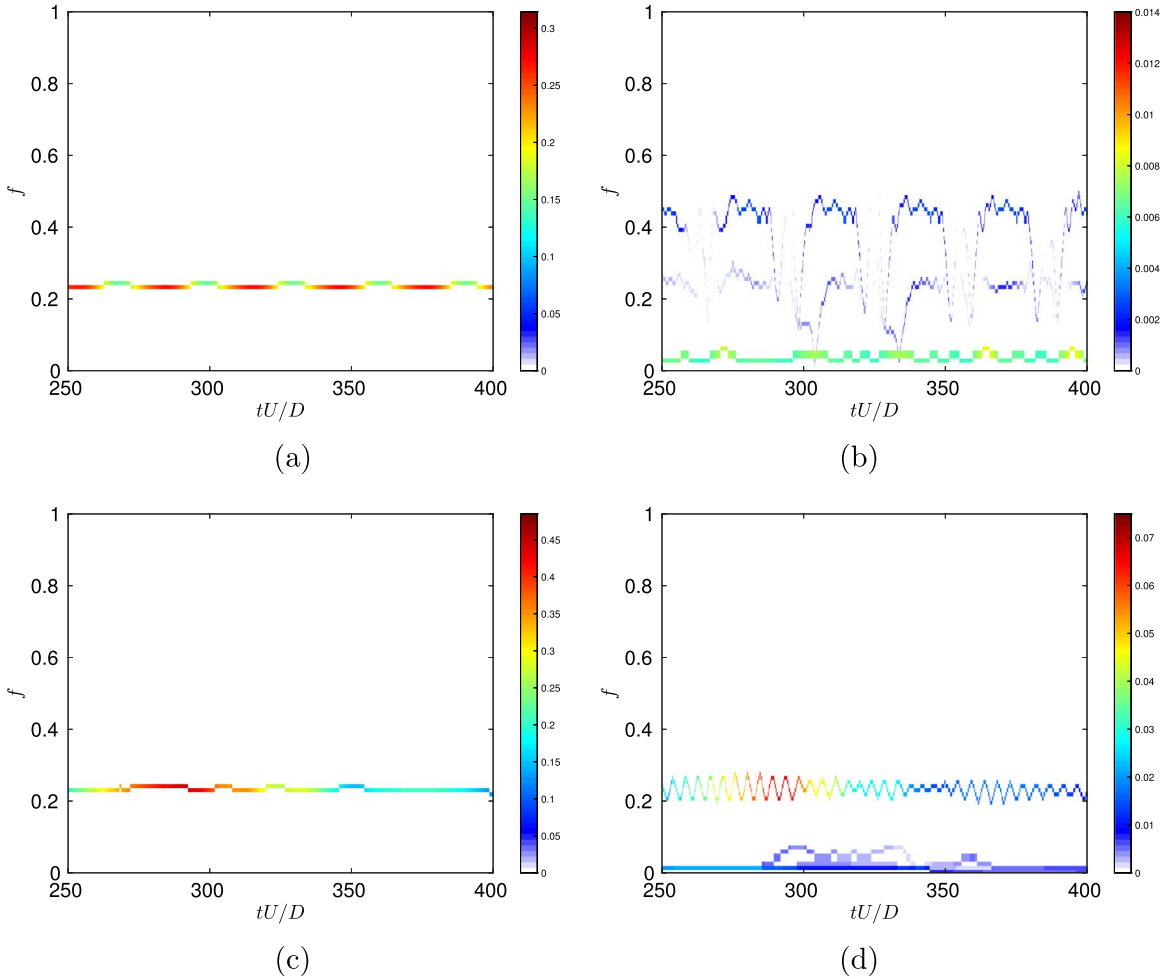


Fig. 23. Evolution of frequency using Hilbert–Huang transform for both isolated (upper) and near-wall (lower) cylinders at $U_r = 4$, $Re = 200$: (a, c) transverse response (b, d) streamwise response. (For interpretation of the references to colour in this figure caption, the reader is referred to the web version of this paper.)

5.1. Amplitudes and forces

For 3D simulations, although it is not possible to cover as many cases as what we have done in 2D due to high computational cost, it can be seen that the 3D results follow similar trends presented by the 2D data. In Fig. 25a, from the 3D simulations, the normalised maximum transverse vibration amplitude, $(A_y)_{max}/D$, of the near-wall cylinder is a bit smaller compared to that of the isolated cylinder. Our $(A_y)_{max}/D$ of the isolated cylinder agrees well with Navrose and Mittal (2013). For 2D simulations for the isolated cylinder at $Re=1000$, $(A_y)_{max}/D$ are quite comparable with 3D results in the pre-lock-in and post-lock-in regimes where the vibration amplitude is relatively small. However, results for $(A_y)_{max}/D$ in 2D are far away from the 3D results in the lock-in region in which relatively large vibration amplitudes are observed. Similar large discrepancies can be observed for the 2D results of the near-wall cylinder in the lock-in range, but fairly close with 3D results in the pre-lock-in and post-lock-in regimes.

With regard to 3D results for the streamwise direction in Fig. 25b, the maximum normalised root-mean-squared streamwise displacement at $U_r = 6$, $(A_x)_{rms}/D$, of the near-wall cylinder is approximately 6 times that of the isolated cylinder, compared to 17 times in the 2D studies at $Re=200$. This means that the wall proximity still largely enhances the streamwise oscillations in 3D, but to a lesser extent compared to 2D. $(A_x)_{rms}/D$ for the isolated cylinder at $Re=1000$ by 2D simulations is over-predicted to a very large extent compared to the 3D results.

In terms of the hydrodynamic forces calculated by 3D simulations, the mean lift force coefficient, $\overline{C_L}$, is enlarged by the wall proximity, shown in Fig. 26a. In Fig. 26b, we find that $\overline{C_D}$ for the near-wall cylinder is larger than that of the isolated cylinder at every U_r considered. The mean drag $\overline{C_D}$ is enhanced by a factor of 2 at $U_r = 4$ and by approximately 10% at other U_r due to the wall proximity. However, this is not the case for 2D results for $Re=200$, as shown in Fig. 4b, where $\overline{C_D}$ are very similar for both configurations. Also, it can be observed in Fig. 26 that 2D simulations for $Re=1000$, at the beginning of

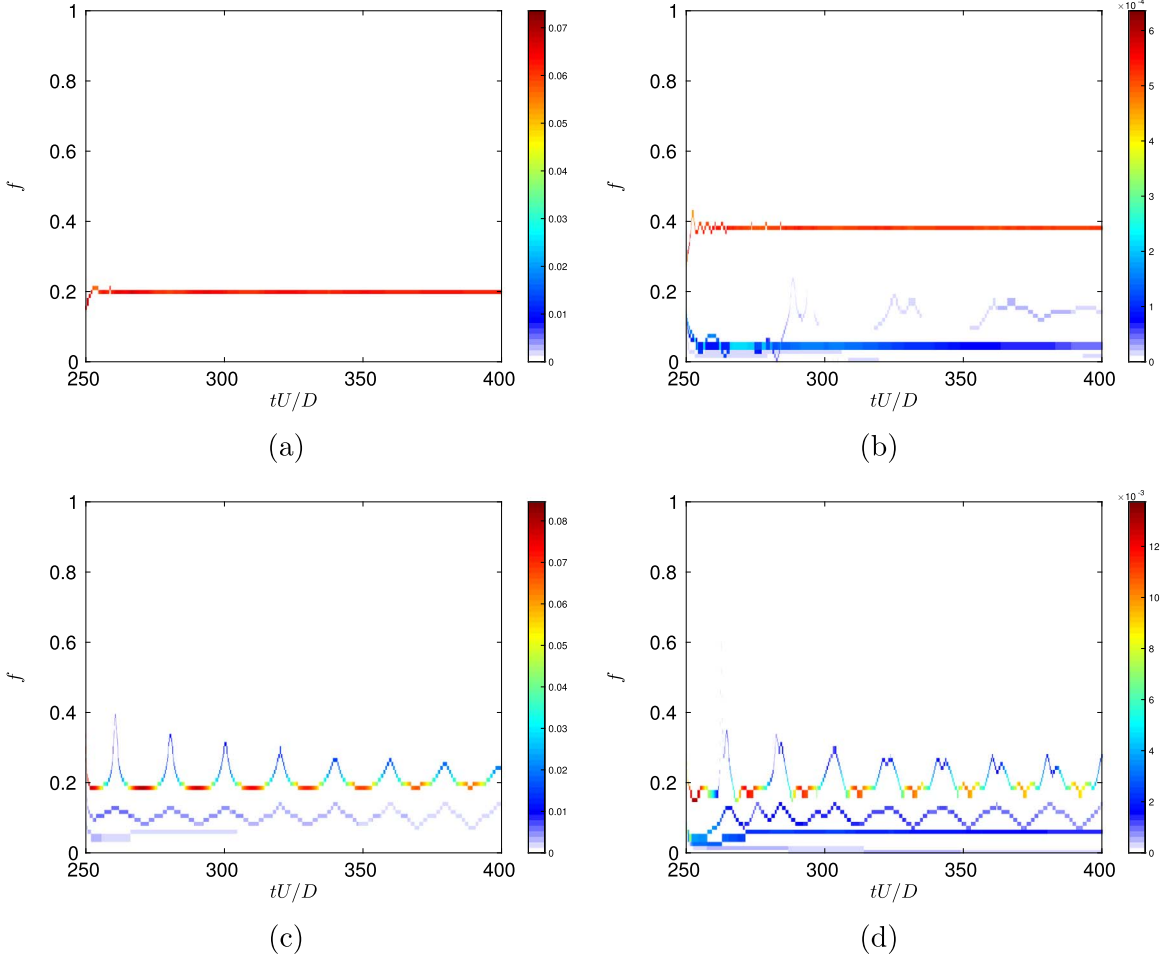


Fig. 24. Evolution of frequency using Hilbert–Huang transform for both isolated (upper) and near-wall (lower) cylinders at $U_r = 6.5$, $Re = 200$: (a, c) transverse response (b, d) streamwise response. (For interpretation of the references to colour in this figure caption, the reader is referred to the web version of this paper.)

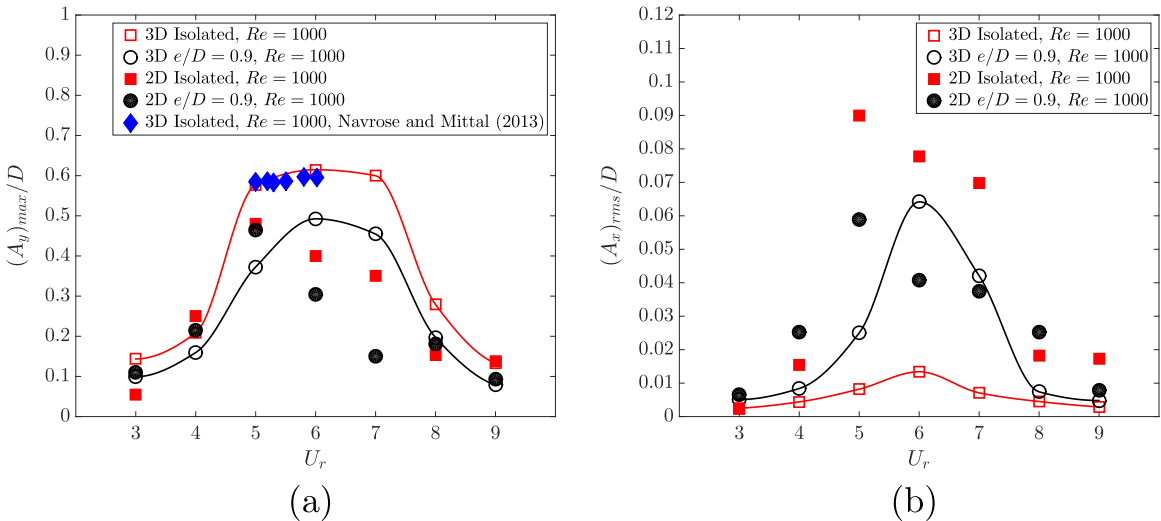


Fig. 25. Vibration amplitudes as a function of reduced velocity U_r for both isolated and near-wall cylinders at $Re = 1000$ in both 2D and 3D: (a) normalised maximum transverse vibration amplitude $(A_y)_{\text{max}}/D$, (b) normalised root-mean-squared streamwise vibration amplitude $(A_x)_{\text{rms}}/D$.

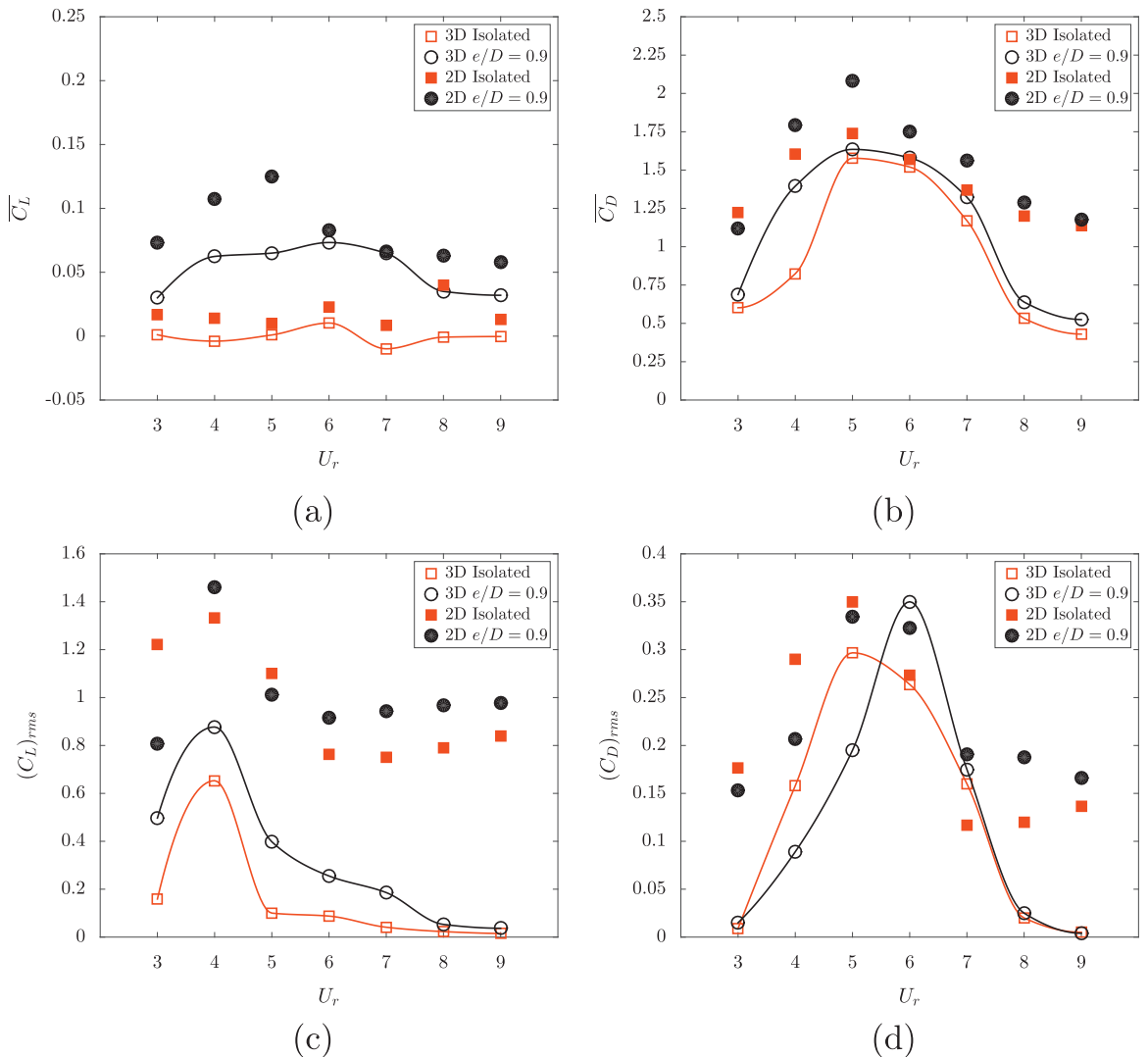


Fig. 26. Force coefficients as a function of reduced velocity U_r for both isolated and near-wall cylinders at $Re=1000$ in both 2D and 3D: (a) mean lift coefficient C_L , (b) mean drag coefficient C_D , (c) root-mean-squared lift coefficient $(C_L)_{rms}$, and (d) root-mean-squared drag coefficient $(C_D)_{rms}$.

Table 5

Comparison of present 3D simulations at $Re=1000$ and $U_r=6$ with [Navrose and Mittal \(2013\)](#) at $Re=1000$ and $U_r=6.2$.

Study	m^*	$m^*\zeta$	$(A_y)_{max}/D$	$(A_x)_{rms}/D$	$(C_L)_{rms}$	\bar{C}_D
Reference	10	0	0.62212	0.00650	0.09944	1.58270
Present	10	0	0.6147	0.0134	0.09	1.52

Table 6

Comparison of $[(A_y)_{max}/D]^*$ by present 3D simulations with experimental studies at similar Re .

Study	Re	$m^*\zeta$	$[(A_y)_{max}/D]^*$
Fujarra et al. (2001)	1000–2500	0.023	0.78
Angrilli et al. (1974)	2500–7000	0.049	0.54
Present	1000	0	0.6147

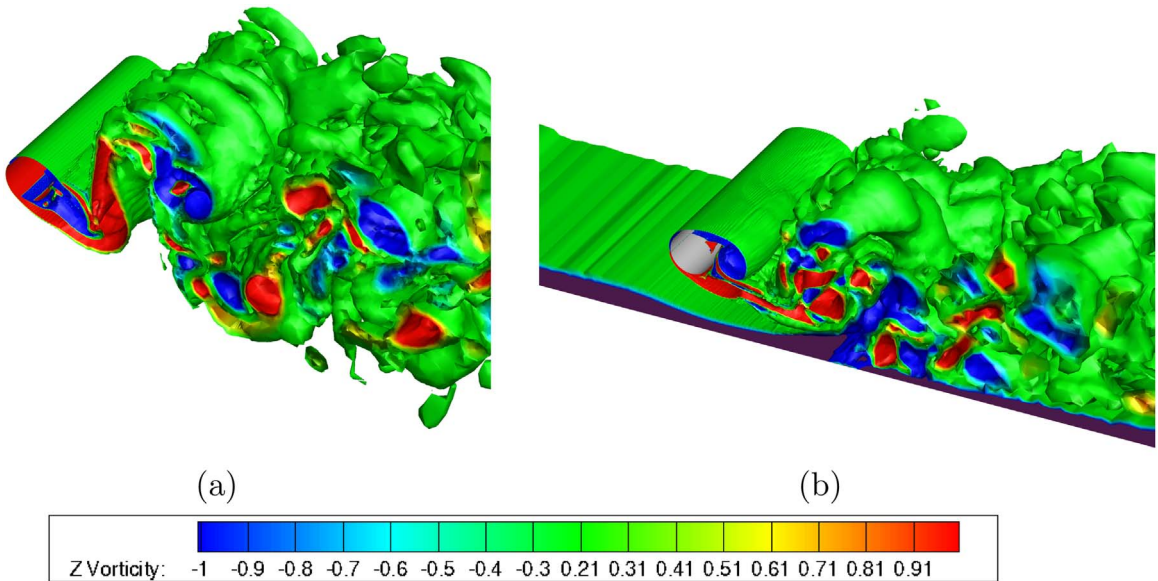


Fig. 27. Isometric view of spanwise vorticity ω_z at $U_r = 5$, $Re = 1000$ for (a) isolated and (b) near-wall cylinders at dimensionless time $tU/D = 250$. Merging of wall vorticity layer with clockwise vortices from top cylinder surface can be seen in the near-wall configuration.

subcritical regime, are not adequate in capturing the hydrodynamic quantities accurately. Force coefficients are in general over-predicted by 2D simulations, and the most extreme case is $(C_L)_{rms}$. In Ong et al. (2010), they also showed that the mean drag coefficient and the root-mean-squared lift coefficient are not correctly calculated by 2D numerical simulations in the subcritical regime ($Re = 1.31 \times 10^4$ in Ong et al., 2010). That is to say, 2D numerical simulations for 2-DoF VIV at $Re=1000$ in the subcritical regime are not valid since the flow is strongly three-dimensional at this particular Reynolds number.

Comparisons of the cylinder responses and hydrodynamic forces from our present 3D computations with the results from the numerical study by [Navrose and Mittal \(2013\)](#) for an isolated cylinder undergoing VIV at $Re = 1000$ are tabulated in [Table 5](#). As can be seen in the table, $(A_y)_{max}/D$, $(C_L)_{rms}$ and $\overline{C_D}$ in our present simulations at $U_r = 6$ agree well with those in [Navrose and Mittal \(2013\)](#) at $U_r = 6.2$. It is also worth mentioning that $(A_x)_{rms}/D$ at $U_r = 6$ in our present study is approximately as large as twice the value at $U_r = 6.2$ from [Navrose and Mittal \(2013\)](#). One possible reason for the discrepancy at $U_r = 6.2$ is that $(A_x)_{rms}/D$ reaches the maximum and becomes sensitive to parameter settings at this particular U_r . At other reduced velocities considered, $(A_x)_{rms}/D$ in our study agrees reasonably well with the results in [Navrose and Mittal \(2013\)](#). For instance, at $U_r = 5$, $(A_x)_{rms}/D$ is approximately 0.008 in [Navrose and Mittal \(2013\)](#), compared to $(A_x)_{rms}/D = 0.0082$ in the present study. For the sake of completeness, the peak normalised maximum transverse vibration amplitude across all reduced velocities considered, $[(A_y)_{max}/D]^*$, is also compared with two experimental studies conducted in similar Re regimes. The experiments are conducted using an elastically-mounted rigid cylinder and a pivoted cylinder in [Angrilli et al. \(1974\)](#) and [Fujarra et al. \(2001\)](#), respectively. The comparison is shown in [Table 6](#).

5.2. Flow fields

To gain a further insight into the flow structures, the three-dimensionality of the wake is further visualised in the following figures in terms of the isosurfaces of spanwise and streamwise vorticities in Figs. 28–30. For the wake structures, similarities and differences can be clearly observed for the isolated and near-wall cylinders.

It is worth noting that there is turbulent activity, particularly in the isosurfaces of spanwise vorticity, ω_z , at downstream of the cylinder, observed in Fig. 27a and b. However, in the near-wake, the isosurfaces of ω_z maintain laminar, yielding an almost two-dimensional wake. This is consistent with the fact that at $Re = 1000$, in the subcritical regime, the boundary layer remains laminar and wake becomes turbulent.

For the spanwise vorticity, ω_z , the counter-clockwise vortices are largely suppressed for the near-wall cylinder, compared to the isolated configuration, owing to the wall proximity effects. Three-dimensional alternate vortex shedding can be observed for the isolated cylinder in Fig. 27a, whereas in the near-wall configuration, the counter-clockwise vortices are suppressed and stretched by the wall in Fig. 27b. Similarly with the mechanism of suppression of bottom shear layer roll-up in 2D, the clockwise vortices shed from the upper surface of the cylinder coalesce with the clockwise wall boundary layer vortices. This coalescing action strengthens the clockwise negative vortices, suppressing the positive ones shed from the lower surface of the cylinder.

We also present the isosurfaces of spanwise vorticity, ω_z , from the top view with two specific values of the contour in Fig. 28, with symmetric values of $\omega_z = \pm 0.5$ plotted in Fig. 28b and asymmetric values of $\omega_z = -3$ and 0.5 plotted in

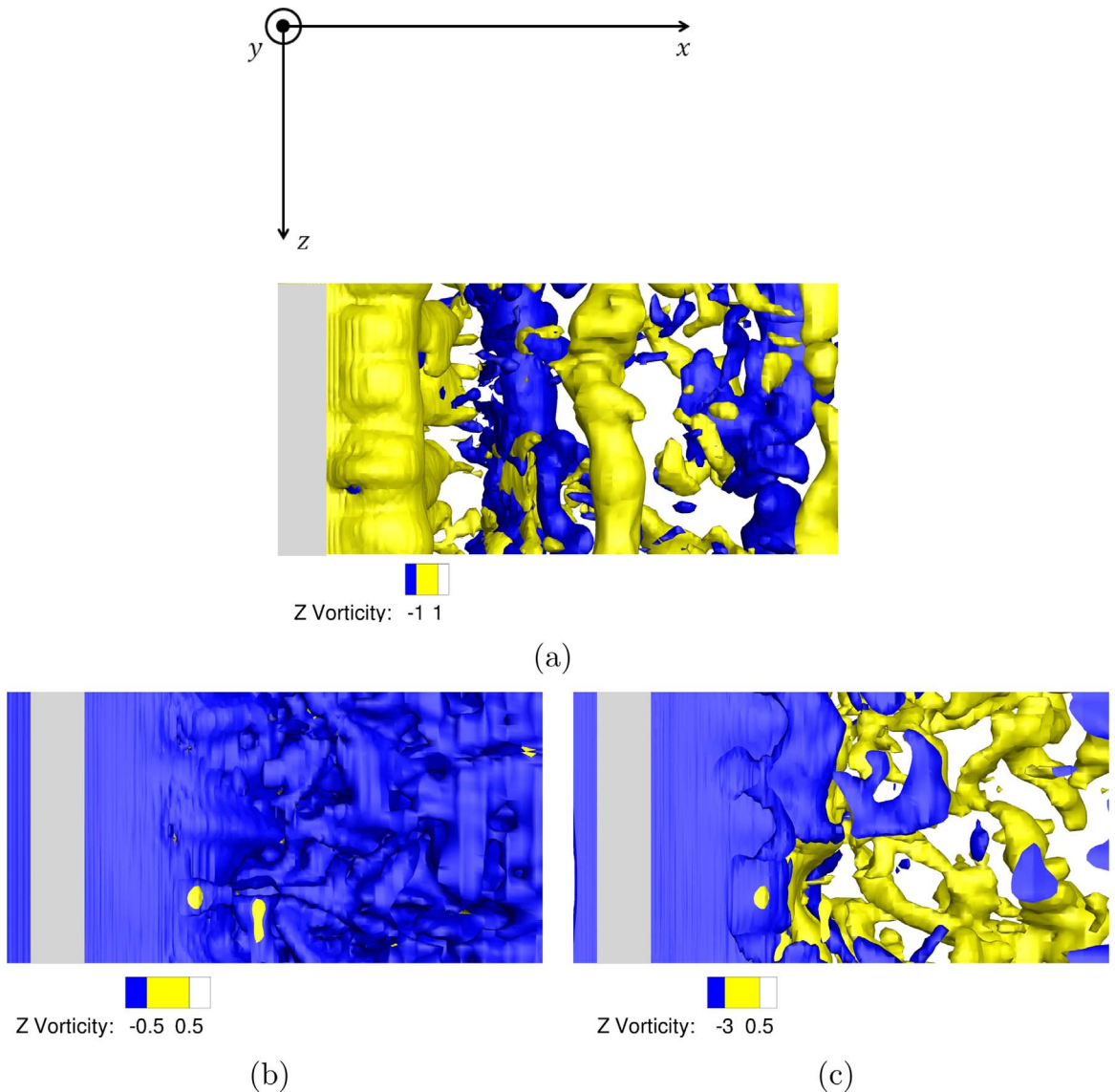


Fig. 28. Top view of spanwise vorticity ω_z at $U_r = 5$, $Re = 1000$ for (a) isolated and (b, c) near-wall cylinders at dimensionless time $tU/D = 250$. Alternate vortex rollers are shed in the isolated configuration. The negative vortices are suppressing positive vortices in the near-wall configuration.

Fig. 28c. As can be seen from the top view in Fig. 28a, regular alternate vortex shedding rollers are observed for the isolated case. However, for the near-wall cylinder, the negative spanwise vortices are largely covering the weak positive ones due to the vortex suppression by the plane wall, shown in Fig. 28b. If the lower limit of the streamwise vorticity is taken at $\omega_z = -3$ to reduce the intensity of negative vorticity, positive vorticity rollers can then be observed under the suppression of negative ones when the asymmetric values of ω_z are taken, as illustrated in Fig. 28c.

The isosurfaces of streamwise vorticity ω_x for both isolated and near-wall cylinders in isometric view are plotted in Fig. 29. The 3D effects in the wake also manifest themselves in the form of streamwise vorticity blobs. Observed from the top view of ω_x in Fig. 30, where two specific values of $\omega_x = \pm 0.5$ are presented, there exists approximately 4.5 wavelengths of the streamwise vorticity blob across the span of the isolated cylinder, i.e. $L/\lambda_{iso} \approx 4.5$ where L denotes the span length and λ_{iso} denotes the wavelength of streamwise vorticity blob for the isolated case. As for the near-wall cylinder, approximately 1.5 wavelengths of the streamwise vorticity blob across the span can be seen, i.e. $L/\lambda_{nw} \approx 1.5$ where λ_{nw} denotes the wavelength of streamwise vorticity blob for the near-wall case. It can be concluded here that the wall proximity largely increases the streamwise vorticity blob by a factor of 3, i.e. $\lambda_{nw}/\lambda_{iso} = 3$. This is because the neighbouring plane wall hinders the communication between the streamwise rib vortices, leading to a much larger wavelength of the blob in the near-wall configuration.

A summary of the wall proximity effects on VIV of an elastically mounted cylinder with 2-DoF in 3D at $Re=1000$ can be

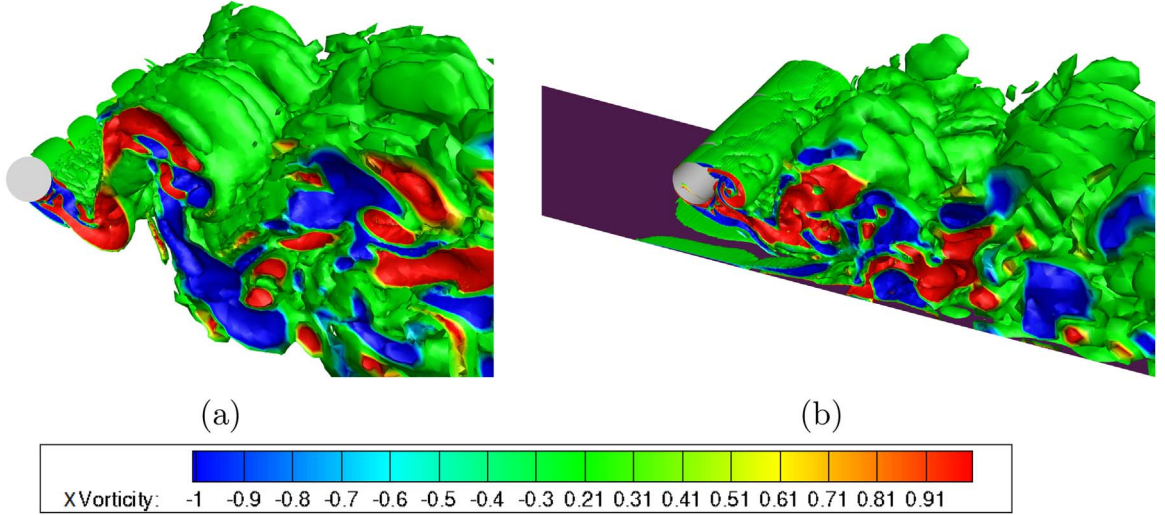


Fig. 29. Isometric view of streamwise vorticity ω_x at $U_r = 5$, $Re = 1000$ for (a) isolated and (b) near-wall cylinders at dimensionless time $tU/D = 250$.

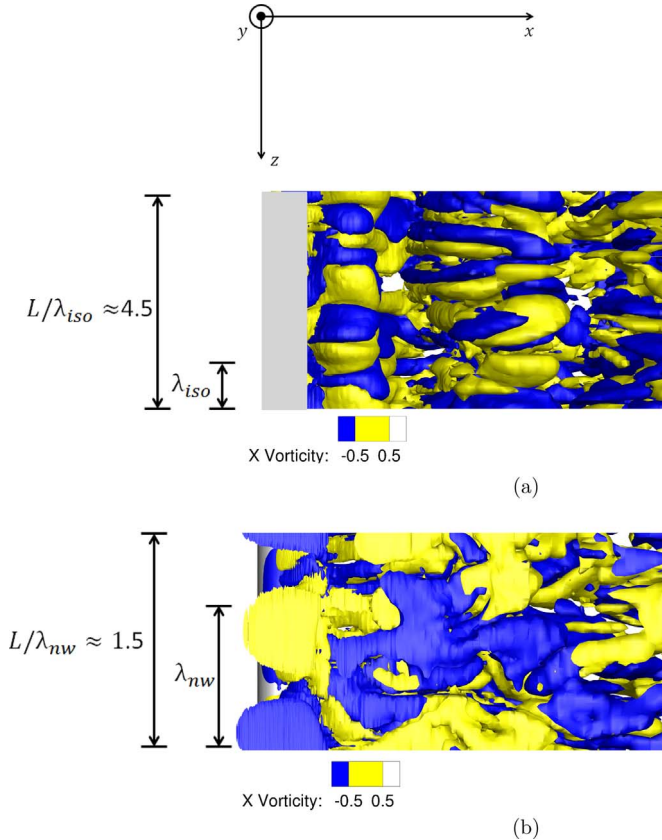


Fig. 30. Top view of streamwise vorticity ω_x at $U_r = 5$, $Re = 1000$ for (a) isolated and (b) near-wall cylinders at dimensionless time $tU/D = 250$. The wavelength of the streamwise vorticity blob is enlarged in the near-wall configuration.

given in the following. The wall proximity increases the mean lift force to a lesser extent compared to 2D results at $Re=200$, while also enhances the mean drag unlike in 2D at $Re=200$. The wall proximity also enhances the streamwise oscillation, similar to 2D. In terms of the flow field, the wall proximity increases the wavelength of streamwise vorticity blob as the wall hinders the communication between the streamwise ribs. Similar to the mechanism of bottom vortex suppression in 2D,

wall boundary layer vortices strengthen the clockwise vortices shed from upper surface of cylinder, stretching and suppressing the counter-clockwise vortices shed from the bottom surface of cylinder.

6. Conclusions

In the present study, 2D and 3D numerical simulations of flow past an elastically mounted circular cylinder with 2-DoF undergoing VIV have been carried out at laminar $Re=200$ and subcritical wake flow $Re=1000$. In our 2D simulations, comparisons have been established between isolated and near-wall cylinders with a gap ratio of $e/D = 0.9$ at $Re=200$ in terms of the hydrodynamic forces, the cylinder responses, the phase relations between forces and displacements, the response frequencies, the cylinder motion trajectories as well as the vorticity fields. We have found that (i) the wall proximity enlarges the mean lift force (transverse force) but has little effect on mean drag force (streamwise force); (ii) the wall proximity promotes the streamwise oscillation by approximately 17 times in comparison to the isolated configuration due to the streamwise frequency lock-in and net energy transfer from the fluid to the cylinder in the pre-lock-in and initial branch of lock-in; (iii) the wall proximity reduces the streamwise vibration frequency by half due to the suppression of bottom shear layer roll-up; (iv) the mechanism of vortex shedding suppression is a cyclic process where the counter-clockwise vortex shed from the bottom surface of the cylinder forces the wall boundary layer to separate and induces a secondary clockwise vortex from the wall boundary layer vorticity which eventually merges with the clockwise vortex shed from the upper surface of the cylinder, strongly suppressing the counter-clockwise vortex roll as a result; (v) in the energy-in phase (at $U_r = 4$) the wall proximity breaks up the periodicity of traces of forces and amplitude responses as found in the isolated configuration, and the resulting beating oscillation is more sensitive in the streamwise direction than the transverse direction, confirmed by detailed HHT analysis; and (vi) in the energy-out phase (at $U_r = 6.5$) the wall proximity does not lead to an apparent non-periodicity of traces of forces and responses, showing that VIV is more sensitive to the interference of the neighbouring wall during energy-in phase than energy-out phase. With regard to 3D simulations, similar comparisons have been established on near-wall VIV. We have found that (i) the wall proximity increases the mean lift force to a lesser extent compared to 2D, and also slightly increases the mean drag force which is different from the 2D scenario; (ii) the wall proximity promotes the streamwise oscillation by approximately 6 times, a much lesser extent compared to 2D; (iii) the wall proximity increases the wavelength of streamwise vorticity blob by a factor of 3 as the neighbouring wall hinders the communication between the streamwise rib vortices; and (iv) similar suppression mechanism of bottom shear layer roll-up is also observed in 3D. Further studies will be considered to evaluate the effects of oblique flows and associated hysteresis effects due to the wall proximity on the phase transitions, namely, the energy-in (initial branch) and the energy-out (lower branch). While the current study has focused on the large gap ratio $e/D \geq 0.9$, there is a need for further numerical study in small gap ratio range where a rebound of vibrating cylinder with the plane wall occurs.

References

- Anagnostopoulos, P., Bearman, P., 1992. Response characteristics of a vortex-excited cylinder at a low Reynolds numbers. *J. Fluids Struct.* 6, 39–50.
- Angrilli, F., Disilvio, G., Zanardo, A., 1974. Hydroelasticity study of a circular cylinder in a water stream. In: Naudascher, E. (Ed.), *Flow-Induced Structural Vibrations*, pp. 504–512.
- Bearman, P.W., Zdravkovich, M.M., 1978. Flow around a circular cylinder near a plane boundary. *J. Fluid Mech.* 89, 33–47.
- Bearman, P.W., 2011. Circular cylinder wakes and vortex-induced vibrations. *J. Fluids Struct.* 27 (5), 648–658.
- Blackburn, H.M., Henderson, R.D., 1999. A study of two-dimensional flow past an oscillating cylinder. *J. Fluid Mech.* 385, 255–286.
- Blackburn, H., Karniadakis, G.E., 1993. Two and three-dimensional simulations of vortex-induced vibration of a circular cylinder. In: *Proceedings of 3rd International Offshore Polar Engineering Conference*, vol. 3, pp. 715–720.
- Brørs, B., 1999. Numerical modelling of flow and scour at pipelines. *J. Hydraul. Eng.* 125 (5), 511–523.
- Brika, D., Laneville, A., 1993. Vortex-induced vibrations of a long flexible circular cylinder. *J. Fluid Mech.* 250, 481–508.
- Carberry, J., Sheridan, J., 2001. Forces and wake modes of an oscillating cylinder. *J. Fluids Struct.* 15, 523–532.
- Carmo, B.S., Meneghini, J.R., 2006. Numerical investigation of the flow around two circular cylinders in tandem. *J. Fluid Struct.* 22, 979–988.
- Carmo, B.S., Meneghini, J.R., 2007. The effect of mass ratio and tether length on the flow around a tethered cylinder. *J. Fluid Mech.* 591, 117–144.
- Chung, J., Hulbert, G.M., 1993. A time integration algorithm for structural dynamics with improved numerical dissipation: the generalized- α method. *J. Appl. Mech.* 60, 370–375.
- D'souza, J.E., Jaiman, R.K., Mak, C.K., 2016. Dynamics of tandem cylinders in the vicinity of a plane moving wall. *Comput. Fluids* 124, 117–135.
- de Langre, E., 2006. Frequency lock-in is caused by coupled-mode flutter. *J. Fluids Struct.* 22, 783–791.
- Fredsøe, J., Sumer, B.M., Andersen, J., Hansen, E.A., 1985. Transverse vibration of a cylinder very close to a plane wall. In: *Proceedings of the Fourth International Symposium on Offshore Mechanics and Arctic Engineering*, vol. 1, pp. 601–609.
- Fredsøe, J., Sumer, B.M., Andersen, J., Hansen, E.A., 1987. Transverse vibrations of a cylinder very close to a plane wall. *J. Offshore Mech. Arct. Eng.* 109, 52–60.
- Fujarra, A.L.C., Meneghini, J.R., Pesce, C.P., Parra, P.H.C.C., 1998. An investigation of vortex-induced vibration of a circular cylinder in water. In: *Proceedings of Fluids Engineering Division Summer Meeting*.
- Fujarra, A.L.C., Pesce, C.P., Flemming, F., Williamson, C.H.K., 2001. Vortex-induced vibration of a flexible cantilever. *J. Fluids Struct.* 15, 51–58.
- Govardhan, R., Williamson, C., 2000. Nodes of vortex formation and frequency response of a freely vibrating cylinder. *J. Fluid Mech.* 420, 85–130.
- Guilmineau, E., Queutey, P., 2002. A numerical simulation of vortex shedding from an oscillating circular cylinder. *J. Fluids Struct.* 16, 773–794.
- Guilmineau, E., Queutey, P., 2000. A numerical simulation of the response of a vortex-excited cylinder. *Proceedings of Flow Induced Vibration Conference*, ed. S Ziada:257–264.
- Huang, W.X., Hyung, J.S., 2007. Vortex shedding from a circular cylinder near a moving wall. *J. Fluids Struct.* 23, 1064–1076.
- Huang, N.E., Wu, Z., 2008. A review on Hilbert–Huang transform: method and its applications to geophysical studies. *Rev. Geophys.* 46.
- Jaiman, R.K., Pillalamarri, N.R., Guan, M.Z., 2016. A stable second-order partitioned iterative scheme for freely vibrating low-mass bluff bodies in a uniform

- flow. *Comput. Methods Appl. Mech. Eng.* 301, 187–215.
- Jaiman, R.K., Guan, M.Z., Miyanawala, T.P., 2016. Partitioned iterative and dynamic subgrid-scale methods for freely vibrating square-section structures at subcritical reynolds number. *Comput. Fluids* 133, 68–89.
- Jensen, B.L., Sumer, B.M., Jensen, H.R., Fredsøe, J., 1990. Flow around and forces on a pipeline near a scoured bed in steady current. *J. Offshore Mech. Arct. Eng.* 112 (3), 206–213.
- Jeon, D., Gharib, M., 2001. On circular cylinders undergoing two-degree-of-freedom forced motions. *J. Fluids Struct.* 15, 533–541.
- Karniadakis, G.E., Triantafyllou, G., 1992. Three-dimensional dynamics and transition to turbulence in the wake of bluff objects. *J. Fluid Mech.* 238, 1–30.
- Khalak, A., Williamson, C.H.K., 1996. Dynamics of a hydroelastic cylinder with very low mass and damping. *J. Fluids Struct.* 10, 455–472.
- Khalak, A., Williamson, C.H.K., 1999. Motions, forces and mode transitions in vortex-induced vibrations at low mass-damping. *J. Fluids Struct.* 13, 813–851.
- Kozakiewicz, A., Sumer, B.M., Fredsøe, J., 1992. Spanwise correlation on a vibrating cylinder near a wall in oscillatory flows. *J. Fluids Struct.* 3 (6), 371–392.
- Lei, C., Cheng, L., Armfield, S.W., Kavanagh, K., 2000. Vortex shedding suppression for flow over a circular cylinder near a plane boundary. *Ocean Engineering* 27, 1109–1127.
- Leontini, J.S., Thompson, M.C., Hourigan, K., 2006. The beginning of branching behaviour of vortex-induced vibration during two-dimensional flow. *J. Fluids Struct.* 22, 857–864.
- Li, Z., Jaiman, R.K., Khoo, B.C., 2016. An immersed interface method for flow past circular cylinder in the vicinity of a plane moving wall. *Int. J. Numer. Meth. Fluids* 81, 611–639. <http://dx.doi.org/10.1002/fld.4198>.
- Lin, C., Lin, W.J., Lin, S.S., 2005. Flow characteristics around a circular cylinder near a plane boundary. In: Proceedings of the Sixteenth International Symposium on Transport Phenomena (ISTP-16).
- Mysa, R.C., Kaboudian, A., Jaiman, R.K., 2016. On the origin of wake-induced vibration in two tandem circular cylinders at low reynolds number. *J. Fluids Struct.* 61, 76–98.
- Navrose, V., Mittal, S., 2013. Free vibrations of a cylinder: 3D computations at $Re=1000$. *J. Fluids Struct.* 41, 109–118.
- Newman, D.J., Karniadakis, G.E., 1995. Direct numerical simulations of flow over a flexible cable. In: Bearman, P.W. (Ed.) *Proceedings of 6th International Conference of Flow-induced Vibrations*, pp. 193–203.
- Ong, M.C., Utnes, T., Holmedal, L.E., Myrhaug, D., Pettersen, B., 2008. Numerical simulation of flow around a marine pipeline close to the seabed. In: *Proceedings of 31st International Conference on Coastal Engineering*, vol.3, pp. 2730–2742.
- Ong, M.C., Utnes, T., Holmedal, L.E., Myrhaug, D., Pettersen, B., 2010. Numerical simulation of flow around a circular cylinder close to a flat seabed at high reynolds number using a $k-\epsilon$ model. *Coast. Eng.* 57, 931–947.
- Papaioannou, G.V., Yue, D.K.P., Karniadakis, G.E., Triantafyllou, M.S., 2006. Three-dimensionality effects in flow around two tandem cylinders. *J. Fluid Mech.* 558, 387–413.
- Prasanth, T.K., Mittal, S., 2008. Vortex-induced vibrations of a circular cylinder at low reynolds numbers. *J. Fluid Mech.* 594, 463–491.
- Prasanth, T.K., Mittal, S., 2009. Vortex-induced vibration of two circular cylinders at low reynolds number. *J. Fluids Struct.* 25, 731–741.
- Puel, F., Victor, X.D.S., 2000. Interaction of wake vortices with the ground. *Aerospace Sci. Technol.* 4, 239–247.
- Raghavan, K., Bernitas, M.M., Maroulis, D.E., 2009. Effect of bottom boundary on viv for energy harnessing at $8 \times 10^3 < Re < 1.5 \times 10^5$. *J. Offshore Mech. Arct. Eng.* 131, 031102.
- Rao, A., Thompson, M.C., Leweke, T., Hourigan, K., 2013. Dynamics and stability of the wake behind tandem cylinders sliding along a wall. *J. Fluid Mech.* 722, 291–316.
- Saad, Y., Schultz, M.H., 1986. GMRES: a generalized minimal residual algorithm for solving non-symmetric linear systems. *SIAM J. Sci. Stat. Comput.* 7.
- Sarpkaya, T., 2004. A critical review of the intrinsic nature of vortex-induced vibrations. *J. Fluids Struct.* 19, 389–447.
- Shiels, D., Leonard, A., Roshko, A., 2001. Flow-induced vibration of a circular cylinder at limiting structural parameters. *J. Fluids Struct.* 15, 3–21.
- Singh, S.P., Mittal, S., 2005. Vortex-induced oscillations at low reynolds numbers: hysteresis and vortex-shedding modes. *J. Fluids Struct.* 20, 1085–1104.
- Sumer, B.M., Fredsøe, J., 2006. *Hydrodynamics Around Cylindrical Structures*. World Scientific Pub Co Inc, Singapore.
- Taneda, S., 1998. Experimental investigation of vortex streets. *J. Phys. Soc. Jpn.* 20, 1714–1721.
- Tang, G., Lu, L., Teng, B., Liu, M., 2013. Numerical simulation of vortex-induced vibration with three-step finite element method and arbitrary Lagrangian-Eulerian formulation. *Adv. Mech. Eng.* 2013, 1–14.
- Taniguchi, S., Miyakoshi, K., 1990. Fluctuating fluid forces acting on a circular cylinder and interference with a plane wall. *Exp. fluids* 9, 197–204.
- Tham, D.M.Y., Gurugubelli, P.S., Li, Z., Jaiman, R.K., 2015. Freely vibrating circular cylinder in the vicinity of a stationary wall. *J. Fluids Struct.* 59, 103–128.
- Tsahalis, D.T., Jones, W.T., 1981. Vortex-induced vibration of a flexible cylinder near a plane boundary in steady flow. In: *Proceedings of the Thirteenth Annual Offshore Technology Conferences*, Houston, pp. 367–386.
- Tsahalis, D.T., 1983. The effect of seabottom proximity of the vortex-induced vibrations and fatigue life of offshore pipelines. *J. Energy Resour. Technol.* 105, 464–468.
- Wang, X.K., Tan, S.K., 2008. Comparison of flow patterns in the near wake of a circular cylinder and a square cylinder placed near a plane wall. *Ocean Eng.* 5–6 35, 458–472.
- Wang, X.K., Tan, S.K., 2013. Vortex-induced vibrations of a neutrally buoyant circular cylinder near a plane wall. *J. Fluids Struct.* 39, 188–204.
- Williamson, C.H.K., Govardhan, R., 2004. Vortex-induced vibrations. *Annu. Rev. Fluid Mech.* 6, 413–455.
- Williamson, C.H.K., Govardhan, R., 2008. A brief review of recent results in vortex-induced vibrations. *J. Wind Eng. Ind. Aerodyn.* 96, 713–735.
- Williamson, C.H.K., Roshko, A., 1988. Vortex formation in the wake of an oscillating cylinder. *J. Fluids Struct.* 2, 355–381.
- Zdravkovich, M.M., 1985. Observation of vortex shedding behind a towed circular cylinder near a wall. In: *Flow Visualization: Proceedings of the Third International Symposium on Flow Visualization*, vol. 3, pp. 423–427.
- Zdravkovich, M.M., 1985. Forces on a circular cylinder near a plane wall. *Appl. Ocean Res.* 7 (4), 197–201.
- Zhang, W., Li, X., Ye, Z., Jiang, Y., 2015. Mechanism of frequency lock-in in vortex-induced vibrations at low reynolds numbers. *J. Fluid Mech.* 783, 72–102.
- Zhao, M., Cheng, L., 2011. Numerical simulation of two-degree-of-freedom vortex-induced vibration of a circular cylinder close to a plane boundary. *J. Fluids Struct.* 27, 1097–1110.
- Zhao, M., Cheng, L., Teng, B., 2007. Numerical modelling of flow and hydrodynamic forces around a piggyback pipeline near the seabed. *J. Waterw. Port Coast. Ocean Eng.* 133 (4), 286–295.
- Zhao, M., Cheng, L., An, H., Lu, L., 2014. Three-dimensional numerical simulation of vortex-induced vibration of an elastically mounted rigid circular cylinder in steady current. *J. Fluids Struct.* 50, 292–311.
- Zhou, D., Tu, J., Bao, Y., 2012. Numerical simulation of two-degree-of-freedom vortex-induced vibration of a circular close to a plane boundary. In: *The Seventh International Colloquium on Bluff Body Aerodynamics and Applications (BBA7)*.